University of Zurich[UZH]

Department of Geography

Remote Sensing Analysis of the Impact of Spruce Bark Beetle (*Ips Typographus*) on Forest Health in the Wildnispark Zürich

GEO 511 Master's Thesis

Author:
Liv Fritsche
12-057-824
Liv.Fritsche@geo.uzh.ch

Supervisor and faculty representative:
Prof. Dr. Alexander Damm
Alexander.Damm@geo.uzh.ch

30th April 2021
Department of Geography
University of Zurich
Switzerland

Abstract

Climate change increases the frequency and severity of heat and drought events, making trees more vulnerable to insect infestation. Spruce bark beetles (*Ips Typographus*) are considered amongst the main disturbances in European forests. Sihlwald is a natural forest located in Zurich, Switzerland, and it is protected since the year 2007, from which date people no longer influenced the natural processes occurring on-site. Extreme weather events have weakened spruce trees and provided breeding ground for insects. The consequence is a rapid dispersal of spruce bark beetles, which has a major impact on the development of the forest. This natural and protected ecosystem is used to study bark beetle dispersal patterns. This thesis proposes an algorithm for the automatic detection of bark beetle affected forest areas and of their spatio-temporal development. Sentinel-2 Level-2A Bottom of Atmosphere (BOA) products are used in order to produce time-series with monthly and yearly resolution. This products exploit the Normalized Difference Water Index (NDWI), which proved to be a suitable index to distinguish between healthy and affected areas. Five products were developed, each of them measuring different traits of the spatio-temporal development of a bark beetle spread. The resulting products demonstrated to be capable of correctly detecting bark beetle infested areas and of mapping their spatio-temporal progression.

Contents

List of Figures

Page

List of Tables

List of Abbreviations

API	Application Programming Interface
BOA	Bottom of Atmosphere
CIR	Colour-infrared
DEM	Digital Elevation Model
diffSuWi	Difference summer to winter
diffToRef	Difference to reference
ESA	European Space Agency
GEE	Google Earth Engine
GIS	Geographic Information System
GPS	Global Positioning System
HistIntensity	Historical Intensity
HistSize	Historical Size
MODIS	Moderate Resolution Imaging Spectroradiometer
MSI	MultiSpectral Instrument
NASA	National Aeronautics and Space Administration, U.S.A.
NDVI	Normalized Difference Vegetation Index
NDWI	Normalized Difference Water Index
NEIS	Naturereignisinformationssystem
NIR	Near infrared
ROI	Region of interest
SAR	Synthetic Aperture Radar
SWIR	Short-wave infrared
TDI	Time Delay Integration
UAV	Unmanned Aerial Vehicle
UoM	Unit of measurement
UTM	Universal Transverse Mercator
VIS	Visible
WGS 84	World Geodetic System 1984
YOD	Year of Death

1 Introduction

1.1 Relevance & Motivation

The increasing occurrence of heat and drought events leads to forests showing severe drought stress, making trees more vulnerable to insect infestation (Abdullah et al., 2019; Matthews et al., 2018; Schuldt et al., 2020; Seidl et al., 2009; Wermelinger, 2020). Climate change furthermore increases the frequency and severity of storm events, providing more breeding material for insects through wind throws (Abdullah et al., 2019; Marini et al., 2017; Potterf and Bone, 2017). Additionally, warmer temperatures prolong the breeding season, leading to increased population sizes (Abdullah et al., 2019; Bentz et al., 2010; Powell and Logan, 2005; Wermelinger, 2004). When it comes to insect disturbances in forest ecosystems, bark beetles are amongst the most critical ones (Biedermann et al., 2019; de Groot and Ogris, 2019; Stereńczak et al., 2020). Spruce bark beetles (*Ips Typographus*) are even considered amongst the main disturbances in European forests (Abdullah et al., 2019; Bentz et al., 2019; Marini et al., 2017). Moreover, bark beetle outbreaks have increased in the past years and are projected to further intensify in the future with climate change (Matthews et al., 2018; Senf and Seidl, 2018). The eruption of a bark beetle infestation can lead to severe economical losses and can have drastic consequences on the affected environment. In extreme cases, ecosystems undergo enormous transformations such as experiencing significant changes in tree species or even shifting from forested to non-forested areas (Millar and Stephenson, 2015; Seidl and Rammer, 2017; Senf and Seidl, 2018).

1.2 Background & State of the Art

Sihlwald is a natural forest located close to Zurich, Switzerland. It is protected since 2007, from which date people no longer influenced the natural processes occurring on-site (Brändli et al., 2020). The storm Burglind/Eleanor in January 2018 (MeteoSwiss, 2018a) has led to an increase of deadwood, and the drought events in 2018 (MeteoSwiss, 2018b) and 2020 (MeteoSwiss, 2021b) have weakened spruce trees. The consequence is a rapid dispersal of spruce bark beetles which has a major impact on the development of the forest. Thus, this natural and protected ecosystem is well suited to study bark beetle dispersal patterns and to identify stimulating factors for the insects. In the case of *Sihlwald*, the bark beetle outbreak is not seen as a disturbance that needs to be counteracted but as a naturally occurring process in a non-directly human-controlled ecosystem. Nonetheless, indirectly induced anthropogenic factors such as climate change inevitably influence ecosystems despite their protected state. Until the recent day, the development of the bark beetle spread in *Sihlwald* has been monitored by rangers. The coordinates of each detected area were assessed by a handheld Global Positioning System (GPS) and registered manually in the the park's internal Naturereignisinformationssystem (NEIS). This ground-based technique is very laborious and the increasing occurrence of bark beetle made the timely, forest-wide monitoring simply impossible.

To tackle such problems more efficiently, we can use optical remote sensing, which is a powerful technology for earth observation that plays a key role in a variety of utilizations. One of the foremost applications is the observation of vegetated areas, which is of crucial importance as it allows to assess the health state of large areas where ground-based monitoring reaches its limits. Airborne, as well as spaceborne data, can be used to monitor areas in the bird's eye view. While airborne imagery usually has the advantage of a good spatial resolution in the scope of centimetres (Kanton Zürich, 2018a, 2020), satellite images are characterized by good temporal resolutions (Jensen, 2009), which is crucial to monitor spatio-temporal changes chronologically (Lillesand et al., 2015).

Highlighting the effects caused by bark beetles is a prerequisite to understand why remote sensing techniques are of great help to detect affected areas. When spruce bark beetles attack their host, spruce trees (*Picea abies L.*), the male insects bore a hole in the outer bark as a first entrance; then, the female beetles bore gateways along the bark where they lay their eggs. When the larvae hatch, they feed on the phloem, the layer below the bark, which is responsible for the transport of down flowing nutrients from the canopy. This feeding process eventually damages the phloem, thus leading to a secondary lack of nutrients in the needles, which causes a gradual decomposition of chlorophyll and a reduction of leaf water content (Nierhaus-Wunderwald and Forster, 2004; Marx and An Der Havel, 2010; Lausch et al., 2013). Optical remote sensing techniques can successfully detect and discriminate the three different stages through which infested trees progress. In the first stage, the green-attack, the tree needles exhibit the usual green colour. Nevertheless, hyperspectral instruments with a red-edge band have the capability to identify this early stage. The following stage, also known as red-attack, can be observed in the visible spectrum as it causes a discolouration of the needles, whose colour changes from green to yellow, and finally to a reddish shade. Lastly, in the gray-attack, the dead foliage falls (Ortiz et al., 2013; Fernandez-Carrillo et al., 2020). In light of the above, an early detection of bark beetle affected trees is crucial when we are interested in containing and counteracting any further spreading. In the literature, particular attention has thus been paid to detecting the green-attack stage, and to distinguishing affected areas from healthy ones by using optical satellite imagery (Jakus et al., 2003; Wulder et al., 2006; Marx and An Der Havel, 2010; Ortiz et al., 2013; Lausch et al., 2013; Fassnacht et al., 2014; Abdullah et al., 2019; Fernandez-Carrillo et al., 2020). However, regardless of how powerful optical satellite remote sensing is, other techniques have been utilized for baseline data retrieval: Synthetic Aperture Radar (SAR) images (Ortiz et al., 2013), airborne optical data-sets (Kautz et al., 2011), or Unmanned Aerial Vehicle (UAV) hyperspectral data (Näsi et al., 2015). The possibility to separate affected areas from healthy ones is crucial and can be used to look at the temporal development of stand areas as done by Meigs et al. (2011). The authors defined six temporal development classes to "characterize spectral trajectories associated with insect activity, stable conditions, and growth" and analyzed Landsat time series over 30 years. Locally variable parameters were studied by Valdez Vasquez et al. (2020) who used optical MODIS images to analyze local variables such as wind speed, temperature and elevation for their importance in the spread patterns of pine bark beetles. Moreover, Simard et al. (2012) studied the landscape context and its influence on tree mortality

through beetle populations. The question of spatio-temporal dispersal patterns of insects has been tackled by Kautz et al. (2011), using yearly airborne colour-infrared (CIR) remote sensing data and a Geographic Information System (GIS) to analyze inter-year changes of bark beetle affected areas.

1.3 Aim & Objective

Although methods for separating infested from healthy areas based on remote sensing data has been thoroughly researched, not equal attention has been paid to assessing the capabilities of mapping and quantifying the spatio-temporal development of spruce bark beetles with remote sensing data. The inquiry of spread patterns allows for a better mechanistical understanding of forest impairment by bark beetles. A time-series with a good temporal resolution builds the baseline for such an inquiry. This thesis aims not only to detect a bark beetle outbreak as early as possible, but to further investigate the spatio-temporal development of spread patterns with different measures. The proposed methods focus on the potential of utilizing time-series of open access optical satellite remote sensing data to retrospectively map and quantify occurring processes in the context of bark beetle infestations. Pixel-based methods and products based on patches of affected regions are introduced to showcase and summarize how the study site has changed from 2017 to 2020.

1.3.1 Research Questions

The questions this thesis aims to answer are as follows:

- Is satellite remote sensing a suitable tool to map the dispersal of bark beetle?
- What measures are suitable to quantify and qualify the dispersal of bark beetles in *Sihlwald*?
- Is it possible to decompose and quantify the contribution of a bark beetle infestation and other natural phenomenons on forest impairment using a remote sensing informed approach?

1.4 Document Overview

The remainder of this thesis is structured as follows. The proposed methods are thoroughly described in Chapter 2. The obtained results are summarized in Chapter 3 and they are thoroughly discussed in Chapter 4. Lastly, a conclusion is given in Chapter 5.

2 Materials and Methods

2.1 Study Site

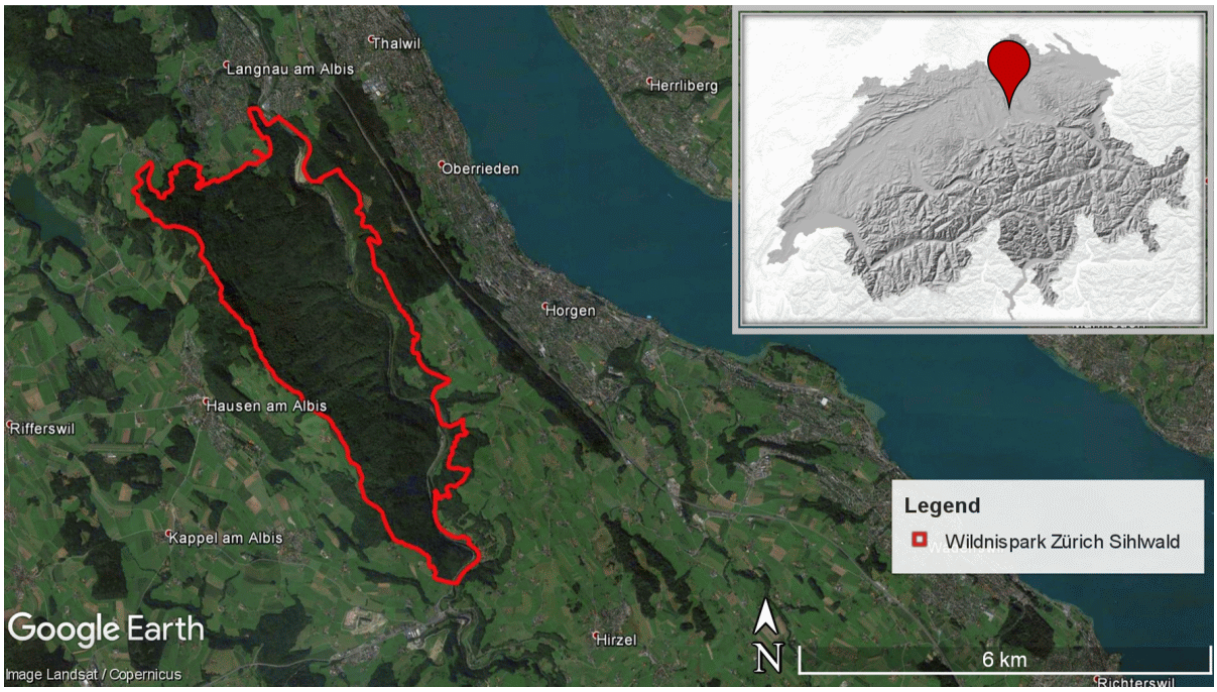

Figure 2.1: Study Site: Wildnispark Zürich Sihlwald. Satellite image: Google Earth Pro, Landsat / Copernicus. Inset map: swisstopo (2019). Perimeter of the Wildnispark Zürich: GIS Wildnispark Zürich (2015).

Sihlwald is one of the largest contiguous beech forests in the Swiss Midlands with a size of 1098 ha (Brändli et al., 2020). The dominant tree species are beech (*Fagus sylvatica*), with a ratio of 46 %, and spruce (*Picea abies*), the most dominant coniferous tree with a ratio of 19 % (Stillhard et al., 2020). Fig. 2.1 depicts the study region, which is located on the west coast of lake Zurich, Switzerland, at coordinates 47°15′25″N, 8°33′30″E, World Geodetic System 1984 (WGS 84). For further analysis, the region of interest (ROI) has been defined as forest area (Kanton Zürich, 2018b) within the perimeters of *Sihlwald* (GIS Wildnispark Zürich, 2015). The site of interest is located in an oceanic climate region, classified as Cfd after Köppen-Geiger with a "warm temperate" main climate, "fully humid" precipitation and "extremely continental" temperature (Kottek et al., 2006). The yearly air temperature average is 9.5 °C and the annual precipitation amounts to 1390 mm while the area receives 1595 h of sunshine per year, resulting in 39 % sunshine (MeteoSwiss, 2021a).

2.2 Satellite Imagery and Spectral Index

2.2.1 Sentinel-2

The main data for the analysis conducted in the scope of this master's thesis stems from the Copernicus Sentinel-2 mission, a constellation of two satellites in a sun-synchronous orbit equipped with a MultiSpectral Instrument (MSI) (Drusch et al., 2012; Martimort et al., 2007, 2012). The data are provided free of charge by the European Space Agency (ESA) (Copernicus, 2014) and was accessed via the Google Earth Engine (Gorelick et al., 2017). The revisit time of 5 days and the 13 spectral bands covering wavelengths from the visible (VIS) spectrum through the near infrared (NIR), and to the short-wave infrared (SWIR) spectrum, make the Sentinel-2 products well suited to answer the research questions. The spatial resolution is spectral band-dependent and its value is either 10, 20 or 60 m. For the analysis herein, the atmospherically corrected Level-2A Bottom of Atmosphere (BOA) reflectance products (Drusch et al., 2012) are used. As the data are provided in the WGS 84 / Universal Transverse Mercator (UTM) zone 32N projection (Roy et al., 2016), all reference data were re-projected and all results are presented in the WGS 84 / UTM zone 32N coordinate system with metres as unit of measurement (UoM).

2.2.2 Setting the Analysis Time Frame

Experts from the *Wildnispark Sihlwald* explained the start of the mass spread of bark beetle in 2018 as follows. Already in the previous years, a few cases of bark beetles had been registered. Nevertheless, the affected areas were always limited to individual trees or very small groups of trees, and did not spread further into the forest. Such a loose occurrence density is normal for any forest. As of 2018, bark beetles have spread through the forest and the affected areas have increased in size continuously (R. Schmidt, personal communication, April 12-14, 2021).
In light of the above, the imagery of 2017 is used as a reference while the successive years set the base for a dispersal study of bark beetle. Leaf foliation of beech and spruce, the main tree species in *Sihlwald*, generally occurs in April and early May, leading to fully developed leaves from June to August, until leaf discolouration starts in September (MeteoSwiss, 2018d, 2019b, 2020b). Fully developed leaves are crucial for this analysis, as they discriminate healthy vegetation from impaired vegetation. Due to the mentioned phenological reasons and cloud-free image availability, the summer months June, July and August for the years 2018–2020 were chosen for the analysis. This time-series over three years allows to map the spatio-temporal development within the time-frame.

2.2.3 NDWI

When a tree is infested with bark beetles, its leaf water content decreases (Nierhaus-Wunderwald and Forster, 2004; Marx and An Der Havel, 2010; Lausch et al., 2013). Thus, a measure for leaf water content is needed in order to map the changes in the forest. This measure can be found in

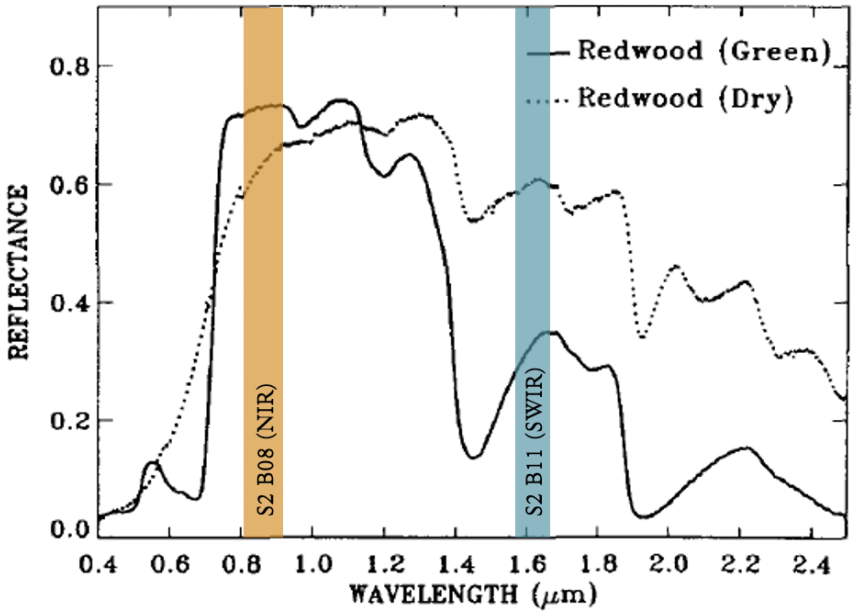

Figure 2.2: Spectra of green and dry vegetation with the highlighted Sentinel-2 Band 08 (NIR) in orange and Band 11 (SWIR) in blue. Adapted after Gao (1996).

the scaled ratio of NIR and SWIR, namely Normalized Difference Water Index (NDWI), which can be expressed as

$$\mathrm{NDWI} = \frac{\mathrm{NIR} - \mathrm{SWIR}}{\mathrm{NIR} + \mathrm{SWIR}}$$

This index has first been introduced by Gao (1996), and it was originally developed to be used with the seven bands of the National Aeronautics and Space Administration, U.S.A. (NASA) satellite Moderate Resolution Imaging Spectroradiometer (MODIS). A graphical interpretation of the NDWI is given in Fig. 2.2. With the aim of adapting the index to Sentinel-2 imagery, the central wavelengths for NIR and SWIR have been shifted to 842 and 1610 nm, respectively (Drusch et al., 2012). Nevertheless, the functioning principle remains the same: in healthy vegetation with a high leaf water content, the liquid water in the canopy causes a considerably stronger absorption in the SWIR wavelengths than in the NIR wavelengths. This contrasting absorption effect in the two observed bands extenuates with decreasing leaf water content and makes the index sensitive to liquid water content of vegetation canopies. The index is dimensionless and ranges between ±1, where high values stand for high leaf water content and high vegetation cover (Gao, 1996). With a spatial resolution of 10 and 20 m in the NIR channel and the SWIR channel, respectively, the computed NDWI products have a spatial resolution of 20 m with a pixel spacing of 10 m.

With its high popularity, the Normalized Difference Vegetation Index (NDVI) depicts an alternative to the used NDWI. The widely used NDVI index measures the greenness of vegetation, depicting the scaled ratio of NIR and red. The NDVI differs from the NDWI, insofar as the red channel is used instead of the SWIR channel. The following arguments led to the decision to use the NDWI instead of the more popular NDVI. Atmospheric aerosol scattering effects are stronger in the VIS spectrum wavelengths than in higher ones, thus making the NDWI more

robust to atmospheric influences (Gao, 1996). Lastly, NDWI exhibits a faster feedback than NDVI for decreasing leaf water content (Gu et al., 2007) which allows to map temporal changes more accurately.

2.3 Data Pre-Processing

2.3.1 Cloud Filtering

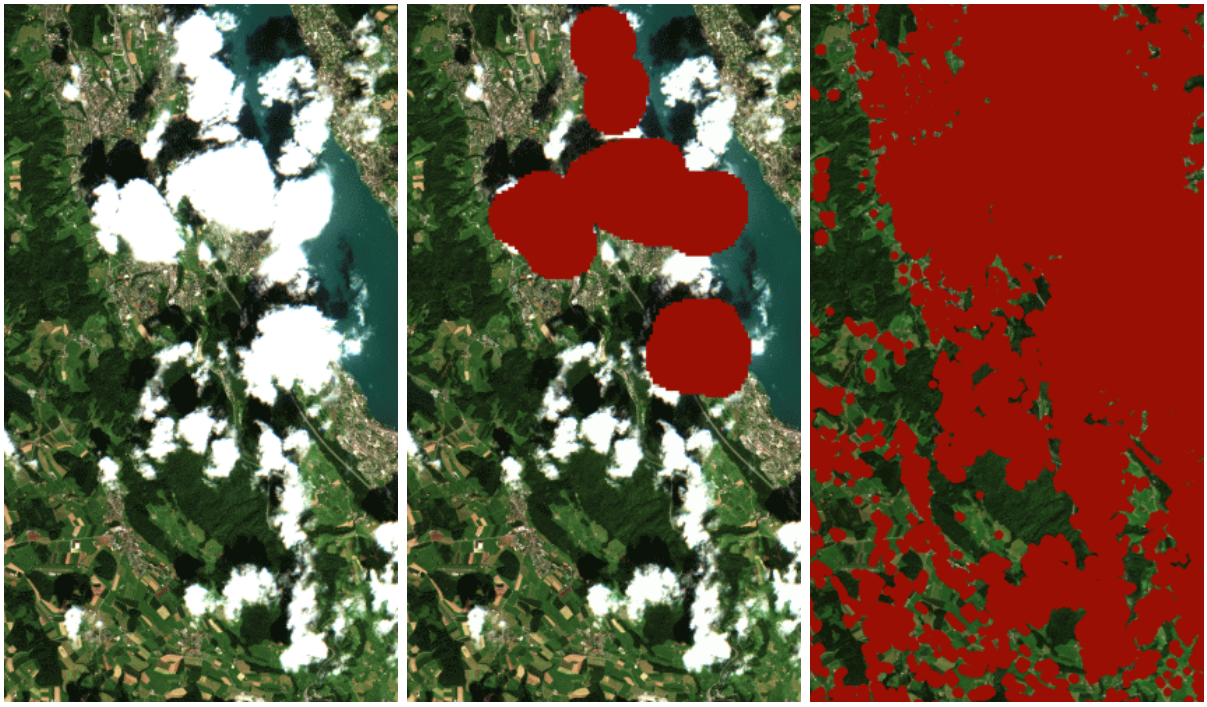

(a) True color composite before cloud filtering **(b)** True color composite with Sentinel-2 cloud mask **(c)** True color composite with cloud mask used in this thesis

Figure 2.3: Comparison of the cloud mask provided by Sentinel-2 and the proposed cloud filtering approach. Masked areas are visualized in red. The image depicts a Sentinel-2 Bottom of Atmosphere reflectance product acquired on 05.08.2017 above *Sihlwald*, retrieved via the Google Earth Engine (Gorelick et al., 2017).

Cloud cover is a crucial factor for the availability of optical, passively acquired remote sensing imagery. Hence, data availability and data quality are considerably dependent on the successful identification, spatial separation and removal of areas affected by cloud cover or cloud shadows. The Sentinel-2 Level 2-A product incorporates a cloud mask; however, its quality has not been found satisfying for the purpose of this thesis because smaller clouds, as well as cloud shadows, are not correctly masked. Hence, in order to detect, map and remove all clouds and their shadows in forest areas, an alternative approach was developed. This approach applies a combination of two independent thresholds, one on the blue and one in the NIR band, as described below. A visual comparison between the Sentinel-2 cloud mask and the one generated by the proposed approach is provided in Fig. 2.3: for the exemplary image (Fig. 2.3a), recorded on 05.08.2017, cloud influence is only roughly included in the Sentinel-2 cloud mask (Fig. 2.3b), while the suggested approach achieves much better results for forested areas (Fig. 2.3c, Fig 2.4).

Table 2.1: Parameters used for the cloud filtering algorithm.

	Thresholding		**Erosion**		**Dilation**	
	Band	Reflectance value	Radius [m]	Iterations	Radius [m]	Iterations
Cloud mask	Blue	> 500	20	1	40	2
Cloud shade mask	NIR	< 1700	30	1	40	2

Setting Thresholds: Clouds have high reflectance values in the VIS region of the electromagnetic spectrum (Bowker et al., 1985). Vegetation, on the other hand, shows low values in the VIS region (Bowker et al., 1985), especially in the blue channel, making it an adequate band for cloud-forest distinction. Fig. 2.4a depicts the Sentinel-2 blue band and emphasizes the aforementioned reflectance differences. Cloud shadows, on the other hand, generally have low reflectance values in the NIR band (Zhu et al., 2015), while for vegetation, the NIR channel is located at the high end of the vegetation red edge feature, thus exhibiting high reflectance values (Lillesand et al., 2015). This behaviour is shown in Fig. 2.4b, which depicts the NIR channel reflectance. These differences suggest to use a threshold in the blue and NIR channel, respectively, to distinguish cloud-induced effects from forest. In light of the above, pixels with BOA reflectance values above 500 in the blue channel are tagged as clouds, and they are visualized in blue in Fig. 2.4c. Pixels with BOA reflectance values below 1700 in the NIR channel are tagged as cloud shadows, and they are visualized in orange in Fig. 2.4d. The threshold values were determined using an empirical approach, and they are summarised in Tab. 2.1. The implementation of the thresholds produces two distinct binary maps, which can be merged together into a single product that highlights cloud-induced effects. This is shown in Fig. 2.4e, where black pixels represent masked areas.

Morphological Opening: The sole use of thresholds leads to an intermediate result which can be improved by implementing an adapted morphological opening on the cloud-effect mask. A morphological opening is an erosion, where pixels are removed from an object boundary, followed by a dilation adding pixels to the boundaries of objects (Khosravy et al., 2017). The result of a morphological opening is the suppression of small-scale filigree structures while the shape of larger objects is preserved. In adaption to a classical morphological opening, the parameters for the erosion and the dilation differ. The use of a larger radius and an additional iteration in the dilation lead to inducing a buffering effect. The motivation for these steps is essentially twofold. On one hand, the threshold mask for cloud shadow effects in the NIR band includes small-sized aggregations of pixels located in steep, shady slope regions, as seen in Fig. 2.4d. To preserve these regions, and to erase single pixel false alarms, filigree details of the combined threshold mask (Fig. 2.4e) are eliminated by performing a morphological erosion. On the other hand, the Sentinel-2 MSI push-broom sensor works in Time Delay Integration (TDI) mode, leading to a temporal offset between the acquisitions of different bands. This introduces a parallax viewing angle between the spectral bands. To align the different spectral bands, they are co-registered during image processing using a Digital Elevation Model (DEM). Nonetheless, these corrections

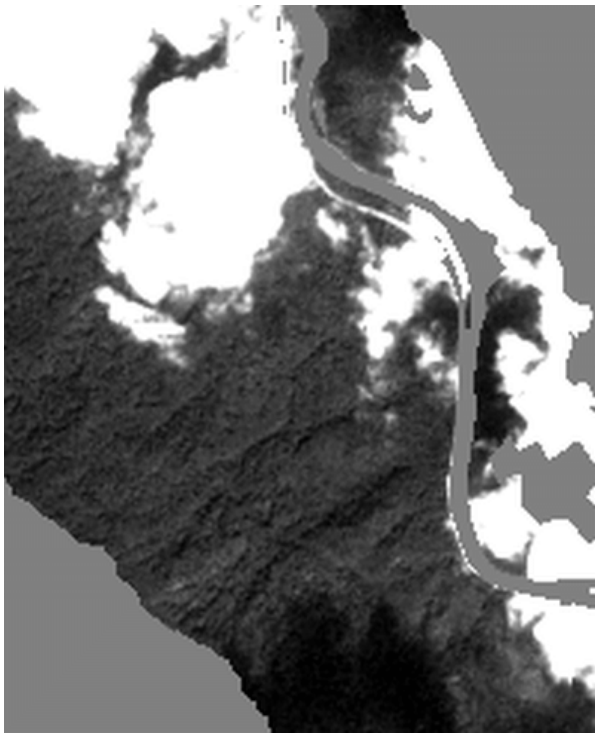

(a) Blue band

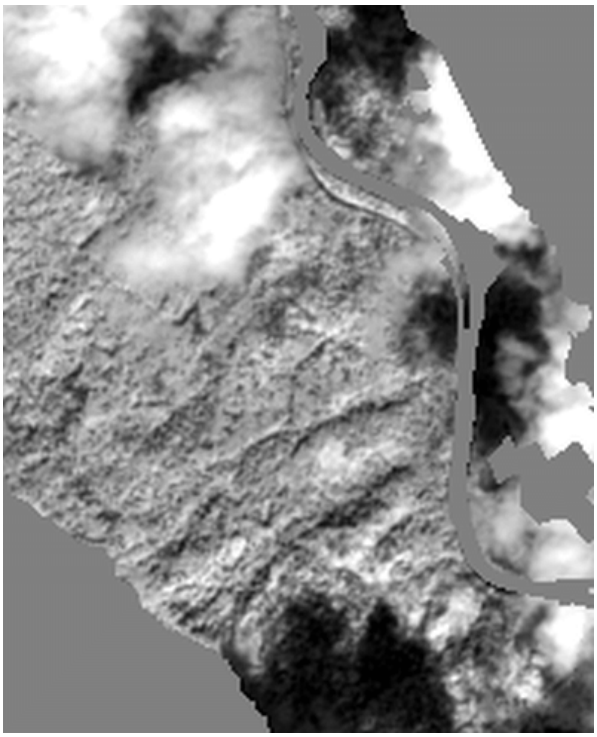

(b) NIR band

(c) True color composite with threshold applied to the blue band

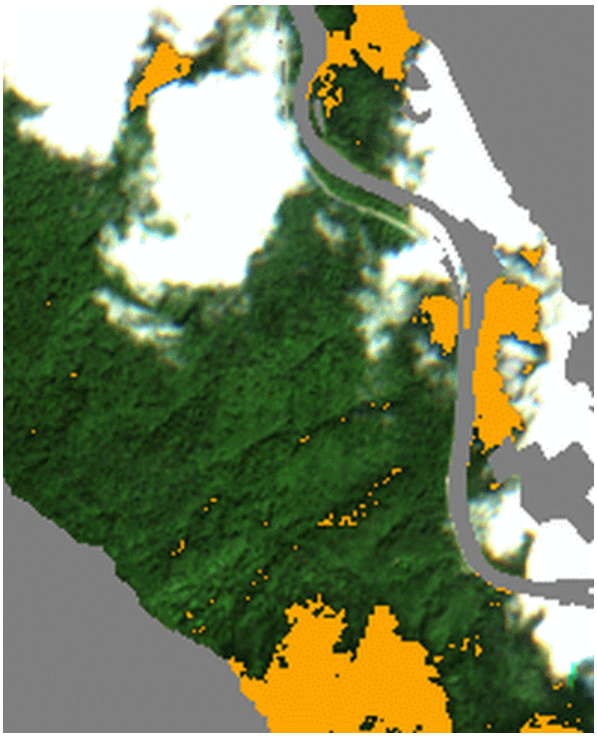

(d) True color composite with threshold applied to the NIR band

(e) Combined threshold mask

(f) Combined threshold mask after morphological opening

(g) True color composite before cloud filtering

(h) True color composite after cloud filtering

Figure 2.4: Visualisation of the used cloud filtering approach, demonstrated on an excerpt of the Sentinel-2 Bottom of Atmosphere reflectance image acquired on 05.08.2017 above *Sihlwald*, retrieved via the Google Earth Engine (Gorelick et al., 2017). Non-forest areas outside the region of interest were masked beforehand (grey).

cannot compensate for the effects of fast moving targets or objects at altitudes higher than the DEM, resulting in a displacement for different spectral bands, which is manifested in the well-known rainbow effects at the periphery of clouds, as seen in Fig. 2.4c. The effect is enhanced with increasing movement speed and altitude of the clouds (ESA, 2012; Frantz et al., 2018; Skakun et al., 2017, 2021). A simple way to remove it is to perform a morphological dilation, resulting in a buffer around the mapped areas.
The parameters for the erosion and dilation constituting the morphological opening of the cloud mask are summarized in Tab. 2.1. The values are chosen so that the erosion step removes most false alarms, yet without erasing important features of the mask. The dilation parameters, which are applied on the resulting mask, are chosen rather broadly to preserve bordering pixels with values close to the original threshold. The wider radius and the additional iteration for the dilation result in a buffer zone of an average of 6 pixels (60 m) and 5 pixels (50 m) for the cloud mask and the cloud shadow mask, respectively, relative to the original threshold mask. As a result of the morphological opening, details of the cloud effect mask disappear, and the main shape of the cloud effect mask is buffered, as shown in Fig. 2.4f. The result of applying the opened mask on all bands is demonstrated on the true color composite, as depicted in Fig. 2.4h: the rainbow effects at the clouds extremities are masked while the pixels located in shady slopes are preserved.

2.3.2 Time Series Construction

Within the analysis time frame, all available Sentinel-2 Level-2A products were masked according to the corresponding cloud masks, and the images with a cloud cover within the ROI above 50 % were removed from the collection. The percentage of the cloud free area for the remaining images is shown in Fig. 2.5. To reduce the dimensionality of the data-set, and to fill the cloud filtered areas, composites were constructed with monthly and yearly temporal resolution.

Monthly Composites: Fig 2.6 shows the procedure for constructing the monthly time series. For each calendar month, the cloud free composite is computed as the pixel-wise median of all available images within the month. The median was preferred over the mean, as the former is more robust against outliers and, therefore, it defines a more stable signal. As the analysis is limited to the months June, July, and August for the years from 2017 to 2020, this results in twelve monthly composites. Consequently, the NDWI is calculated per monthly composite and added as an additional band. As mentioned before, 2017 is determined as the reference year. To compensate for seasonal effects such as sun illumination angle and phenology, each monthly composite of the following years is normalized with respect to the corresponding monthly composite of the reference year. That is, for a given month and year of interest, the 2017 composite of the corresponding month is subtracted. Hence, nine monthly NDWI diffToRef composites are available from 2018 to 2020.

Yearly Composites: The yearly products are generated in a similar fashion to the monthly composites. For each pixel, the resulting value is obtained as the median of the cloud free

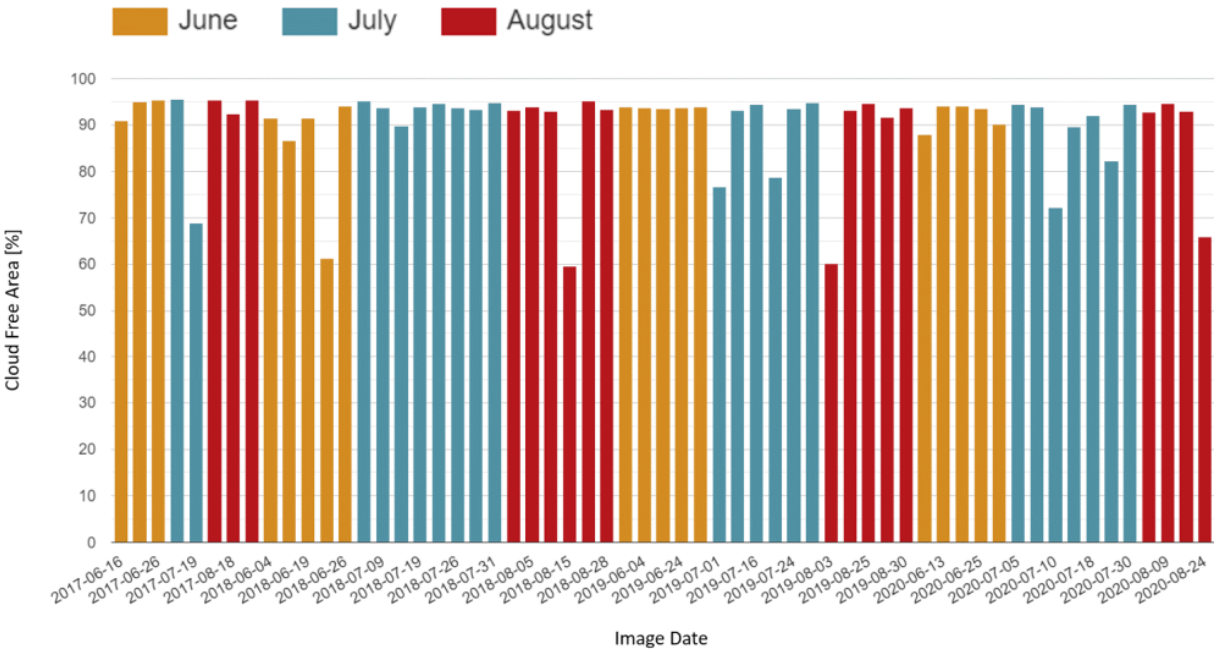

Figure 2.5: Sentinel-2 imagery used for the analysis. Each bar is related to a satellite image. The color codes the calendar month, whereas the height of the bar indicates the percentage cloud-free area.

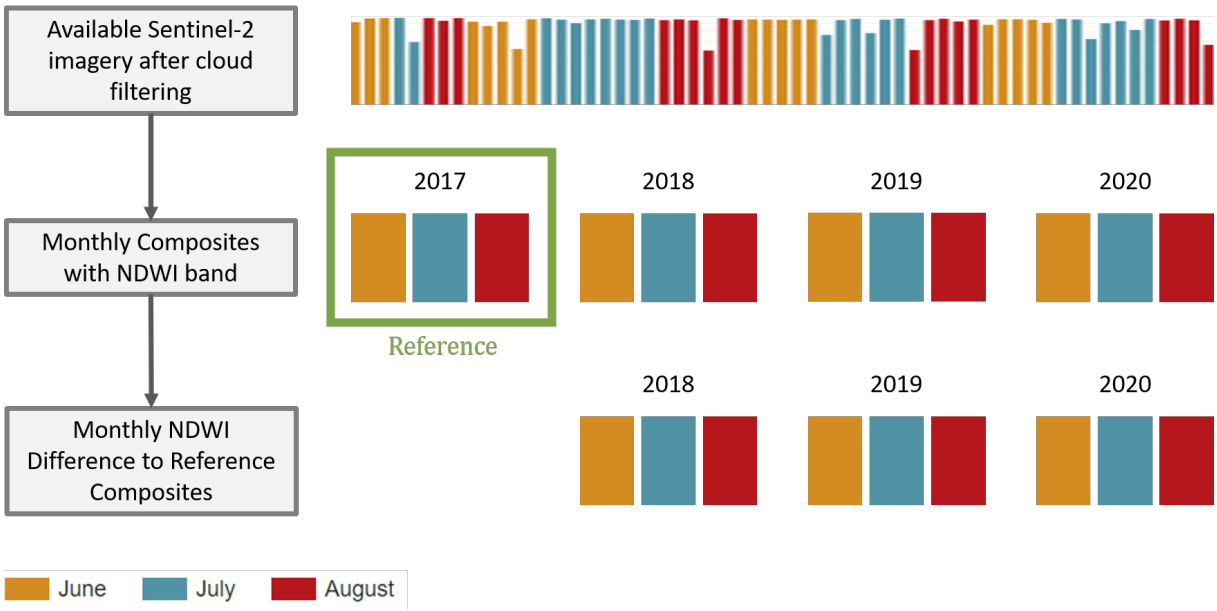

Figure 2.6: Visualisation of the time series construction consisting of nine monthly NDWI diffToRef Composites for the months June, July, and August from 2018 to 2020 with 2017 as the reference.

available imagery within the year. That is, the yearly products comprise the median value of the months June, July and August of the year of interest. Hence, the NDWI is computed for each yearly composite. Lastly the 2017 composite is subtracted from the yearly composites for the years 2018–2020, therefore producing three final yearly NDWI diffToRef composites.

2.4 Preliminary Measures for the Product Computation

2.4.1 Overall Mask

For both time series (i.e., monthly and yearly), an overall-mask was computed in order to preserve only those pixels being represented in all composites contributing to the product. That is, in the final product, the non-masked pixels values were obtained by processing the same number of monthly/yearly composites.

2.4.2 Distinguishing Affected Pixels From Healthy Pixels

To allow for an easier and more intuitive interpretation, some of the measures use a threshold to distinguish between affected and non-affected pixels. When thresholding an input image characterized by a continuous set of values, the resulting output is a binary map. Though being a huge simplification, this step crucially reduces data complexity while classifying the input pixels into two distinct groups. The threshold is a function of the most recent monthly NDWI diffToRef composite (August 2020 - August2017), and its value (i.e., -0.09) was derived by combining empirical evidences with a histogram-informed approach. Hence, all pixels with an NDWI diffToRef value < -0.09 are classified as affected pixels. For consistency reasons, the same threshold is used for all composites and products introduced below.

2.5 Tree Types in Sihlwald

With an intensive spruce bark beetle spread in *Sihlwald*, spruce trees are expected to be strongly represented among the health-impaired trees. Furthermore, spruce trees represent the majority of all evergreen trees in *Sihlwald* (Brändli et al., 2020; Stillhard et al., 2020). Thus, the majority of all affected pixels is expected to be found in evergreen areas. To verify this assumption, affected regions are compared to a map, differentiating in between evergreen and deciduous pixels.
The baseline for this tree type discrimination is the difference summer to winter (diffSuWi) data-set. The winter data-set incorporates the median of all cloud free imagery from 15.10.2017 until 15.04.2018. The winter data-set was subtracted from the summer data-set, comprising the median of all cloud free imagery from June, July and August 2017. A threshold was used in order to make the diffSuWi data-set suitable for discriminating between evergreen and deciduous areas. Its value was derived in a similar fashion to what was proposed in Bazi et al. (2007), and Huang and Chau (2008). The implemented method is based on two main assumptions: a) the region of interest is subdivided into two main classes (i.e., evergreen and deciduous) and b) the variables to be distinguished are normally distributed. Under such circumstances, the diffSuWi histogram can be accurately described with a linear mixture model of two Gaussian distributions,

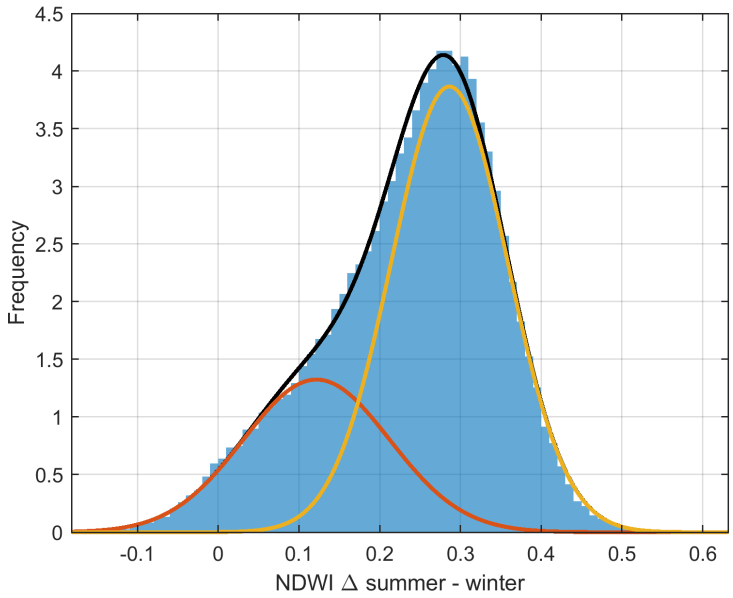

Figure 2.7: Histogram of the NDWI summer - winter difference and resulting distributions.

as visualized in Fig. 2.7. The blue histogram exhibits the distribution of the NDWI diffSuWi values. The yellow and red lines represent the two Gaussian distributions while the black line represents their sum. Although this approach is a simplification, the intersection point of the two normal distributions yields a rough estimate of the threshold (i.e., 0.17) that needs to be used to separate the two classes.

2.6 Software

The results presented herein were obtained by using different software. Satellite data was accessed via the Google Earth Engine (GEE) data catalog using the cloud-based GEE platform (Gorelick et al., 2017). GEE was handled via the JavaScript Application Programming Interface (API), designed for parallel processing, allowing an efficient evaluation of time series with a relatively low computational effort per image (Gorelick et al., 2017). Nevertheless, the available computational power for an individual user is limited by GEE. Without a upscale on request, the limited computational power reaches its limits when dealing with computationally more laborious tasks such as morphological functions (Section 2.3.1 and Section 3.2.1) or the patch analysis (Section 3.2) (Sidhu et al., 2018). GEE was used to perform cloud filtering (Section 2.3.1), time series construction (Section 2.3.2) and to compute different products, including the patch definition (Section 3.2.1), the Year of Death (YOD) map (Section 3.1.1), the Age map (Section 3.1.2) and the Intensity map (Section 3.1.3). Further analysis and data examination were performed in MATLAB (The MathWorks Inc., 2019). It was used, amongst others, to visualize the pixel-based products in Section 3.1 and for histogram and box plot visualizations. Additionally, QGIS (QGIS Development Team, 2018) was used for data comparison and visualization.

3 Results

This thesis proposes different measures to map and quantify dispersal patterns of bark beetles. The NDWI diffToRef time-series, constructed as described in Section 2.3.2, can be used to monitor how affected areas change over time. All measures are obtained on the basis of the time series of NDWI composites either with monthly or yearly resolution.

3.1 Pixel-based Products

In the following, the pixel-based products are depicted. All measures are presented in such a way that a brighter colour (i.e., yellow) corresponds to a stronger or older damage.

3.1.1 Year of Death Map

The YOD product is computed as a function of the yearly NDWI diffToRef time series. In order to recognize affected pixels, each yearly composite is thresholded as described in Section 2.4.2. For a given year, the corresponding yearly product is a binary map identifying those pixels that were detected as unhealthy for the first time in the year of interest. The YOD map combines the binary maps for the years 2018, 2019 and 2020, thus informing when a given pixel was detected as unhealthy for the very first time.
The YOD map and the related histogram are illustrated in Fig. 3.1a and Fig. 3.1b, respectively. While in 2018 and 2019 the size of the newly-affected area is similar (i.e., roughly 10 ha), it then increases drastically in 2020 to 6000 pixels, representing six times the area of the previous year. When analysing Fig. 3.1a, it is evident that most of the affected pixels are located in the north part of the *Sihlwald* forest (i.e., above Northing coordinate 5'234'500).

3.1.2 Age Map

The Age product is based on the monthly NDWI diffToRef time series. The threshold described in Section 2.4.2 is applied on each monthly composite. The Age map exhibits the pixel-wise sum of the affected composites.
The Age map is visualized in Fig. 3.2a: the possible values are discrete, integer and range between 0 and 9, where non-0 values represent areas which have been marked as affected at least once. The histogram of Fig. 3.2b approximates the distribution of the variable Age. Since the large majority of the pixels within the ROI are healthy (i.e., their Age value is 0), the histogram is computed only on the pixels with non-null Age value. From a visual analysis of Fig. 3.2b, it appears clear that the number of pixels gradually decreases with increasing Age values.

3.1.3 Intensity Map

Based on the monthly time series, the Intensity map cumulates the NDWI diffToRef values for each pixel, resulting in the cumulative NDWI anomaly. As the main focus lies on the detection of

affected regions, only negative values are conserved while positive values are set to zero. The lower (i.e., more negative) the cumulative NDWI anomaly, the higher the Intensity. Henceforward, a high Intensity value indicates a low cumulative NDWI anomaly, and thus a severe degradation. The Intensity map is depicted in Fig. 3.3a. This product is obtained on the the basis of the negative cumulative NDWI anomaly. The values are continuous and range in between -4.06 and 0. The corresponding histogram of Fig. 3.3b is a *quasi*-monotonically increasing function: that is, neglecting few fluctuations at the lowest Intensity values, it shows a continuously increasing trend. The large majority of the Intensity values, the 99.9 % of the entire population, falls between -1.84 and 0.

3.1.4 Close Ups

The Age, Intensity and YOD map are further investigated by analysing five different areas of interest, which were picked on the basis of their meaningfulness. An overview of the chosen locations is given in Fig. 3.4, whereas the resulting products are summarized from Fig. 3.5 to Fig. 3.9. For validation purposes, the false color infrared orthophotos of summer 2018 (Kanton Zürich, 2018a) and summer 2020 (Kanton Zürich, 2020) are depicted in subplot a) and b), respectively. All the 2018 orthophotos were recorded on August the 27-th (Kanton Zürich, 2018a), whereas the ones from 2020 were recorded between the 9-th and 10-th of August (Kanton Zürich, 2020). The Age, Intensity, and YOD close-ups are summarized from subplot c) to e).

Area 1: The products for Area 1 (A1) are summarized in Fig. 3.5. The area is located west of *Tobel* (field name from swisstopo (2020)) in the norther part of *Sihlwald*, and it is particularly significant as it shows one of the first outbreak areas of bark beetles in *Sihlwald* (R. Schmidt, personal communication, April 12, 2021). In the 2018 orthophoto (Fig. 3.5a), some dead trees can be seen in the upper right corner, and a fewer amount can be recognized in the lower left quadrant. In 2020 (Fig. 3.5b), the number of dead trees has substantially increased up to the point where almost all coniferous trees are affected. The corresponding Age and YOD map, which are summarized in Fig. 3.5c and Fig. 3.5e, respectively, show high peaks (i.e., brighter colors) in the same areas.

Area 2: Fig. 3.6 visualizes a close-up view of Area 2 (A2), which lies close to *Cholbenholz* (field name from swisstopo (2020)) in the northern part of *Sihlwald*. A2 represents a meaningful example of a temporal spread pattern of affected trees. The 2018 orthophoto (Fig. 3.6a) shows almost no affected trees while the 2020 aerial image (Fig. 3.6b) exhibits a spread equally distributed along the east-west axis. Age (Fig. 3.6c) and Intensity (Fig. 3.6d) values decrease from east to west. The main difference between the two products is represented by the small hot-spot visible in the mid-eastern part of the Intensity image. YOD (Fig. 3.6e) values are higher in a hot-spot located in the eastern part of the excerpt, and they are generally more scattered than the Age values. Unlike for 2019 and 2020, the 2018 detections define quite small areas (i.e., one or two pixels) and they appear to be randomly scattered over the whole excerpt.

Area 3: A close-up view of Area 3 (A3), located in the southern part of *Sihlwald* between *Egliboden* and *Im roten Meer* (field names from swisstopo (2020)), is given in Fig. 3.7. The area of interest appears to be mainly non-affected in 2018 (Fig. 3.7a), and it then progresses to develop a rather sparse distribution of affected trees in 2020 (Fig. 3.7b). The Age (Fig. 3.7c), Intensity (Fig. 3.7d) and YOD (Fig. 3.7e) product present the most prominent contributions in the upper right quadrant. For all these measures, the affected pixels are much more scattered than in the previous examples, in accordance with the available ground measurements.

Area 4: The products of an additional area of interest, namely Area 4 (A4), are depicted in Fig. 3.8. A4 is located in the southern part of Sihlwald, nearby *Schönboden* (field name from swisstopo (2020)). This excerpt is of particular interest due to its peculiar initial state. In 2018 (Fig. 3.8a), a group of lying trees is clearly recognizable in the upper right corner, whereas the remaining area appears to be healthy. Later on, in 2020 (Fig. 3.8b), the aforementioned lying trees are still present, though not being easily recognizable due to secondary vegetation. Nevertheless, other patches of affected trees can be detected. For all the available products, Age (Fig. 3.8c), Intensity (Fig. 3.8d) and YOD (Fig. 3.8e), the most prominent contributions are located in the upper right part of the excerpt.

Area 5: Lastly, in Fig. 3.9, the results of Area 5 (A5) are summarized. The area is located in the southern part of *Sihlwald*, close to *Bruggrain* (field name from swisstopo (2020)). The region exhibits a peculiar straight line of affected trees running from north-east to south-west which can likewise be recognized in the photograph in Fig. 3.10, taken in August 2019. While only very few isolated brown trees can be seen in 2018 (Fig. 3.9a), the eye-catching line, as well as some more scattered trees along the forest border in the eastern part of the excerpt, are affected in 2020 (Fig. 3.9b). Age (Fig. 3.9c) and YOD (Fig. 3.9e) values spike within the line as well as in several pixels in the lower right quadrant. The Intensity map (Fig. 3.9d) shows high values in the same regions.

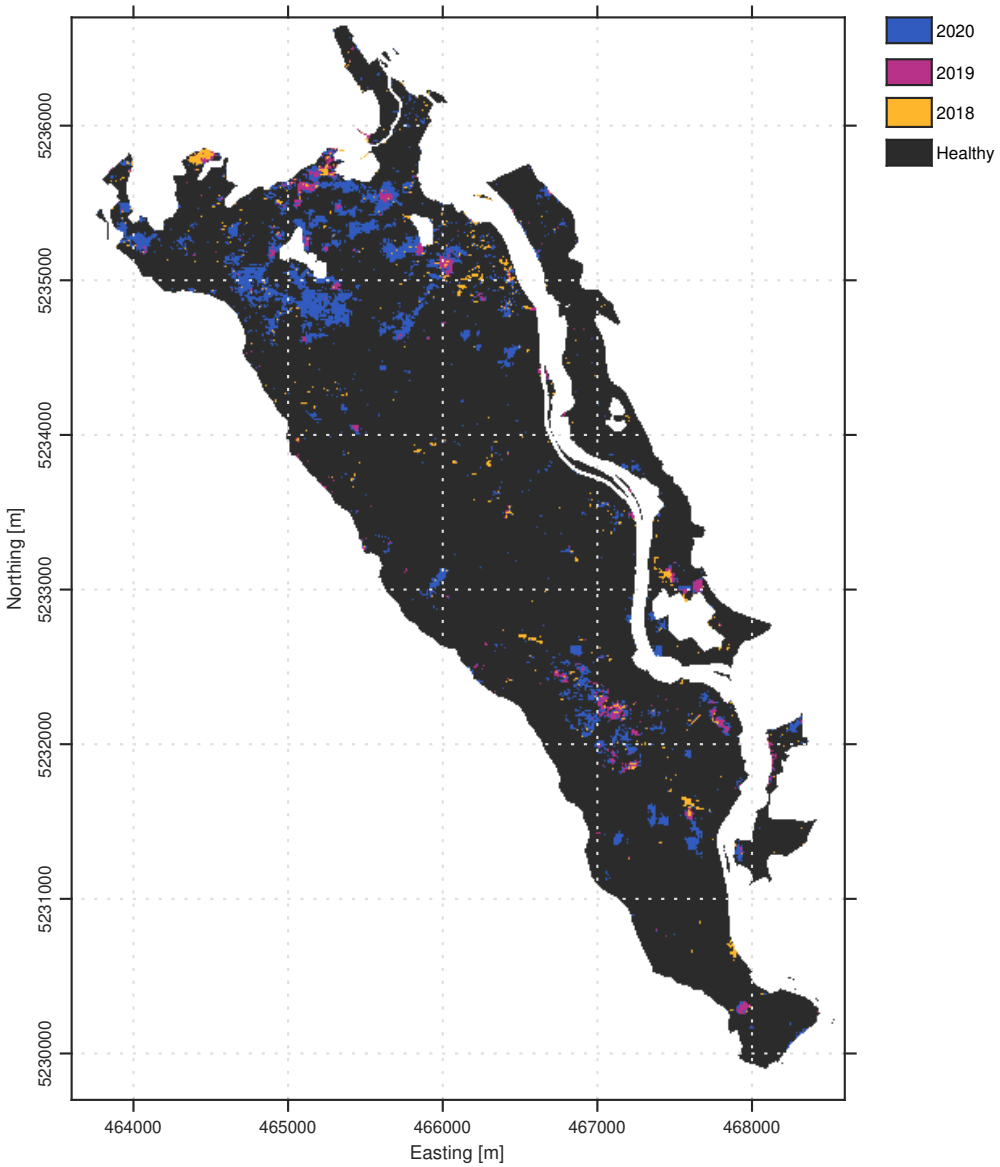

(a) YOD map. Coordinates in WGS 84 / UTM zone 32N, UoM: m.

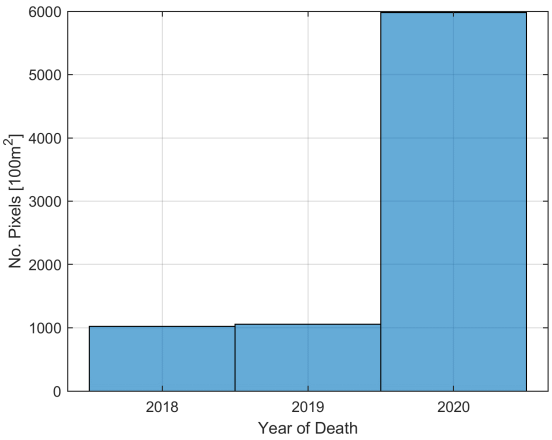

(b) Histogram of YOD map.

Figure 3.1: YOD product.

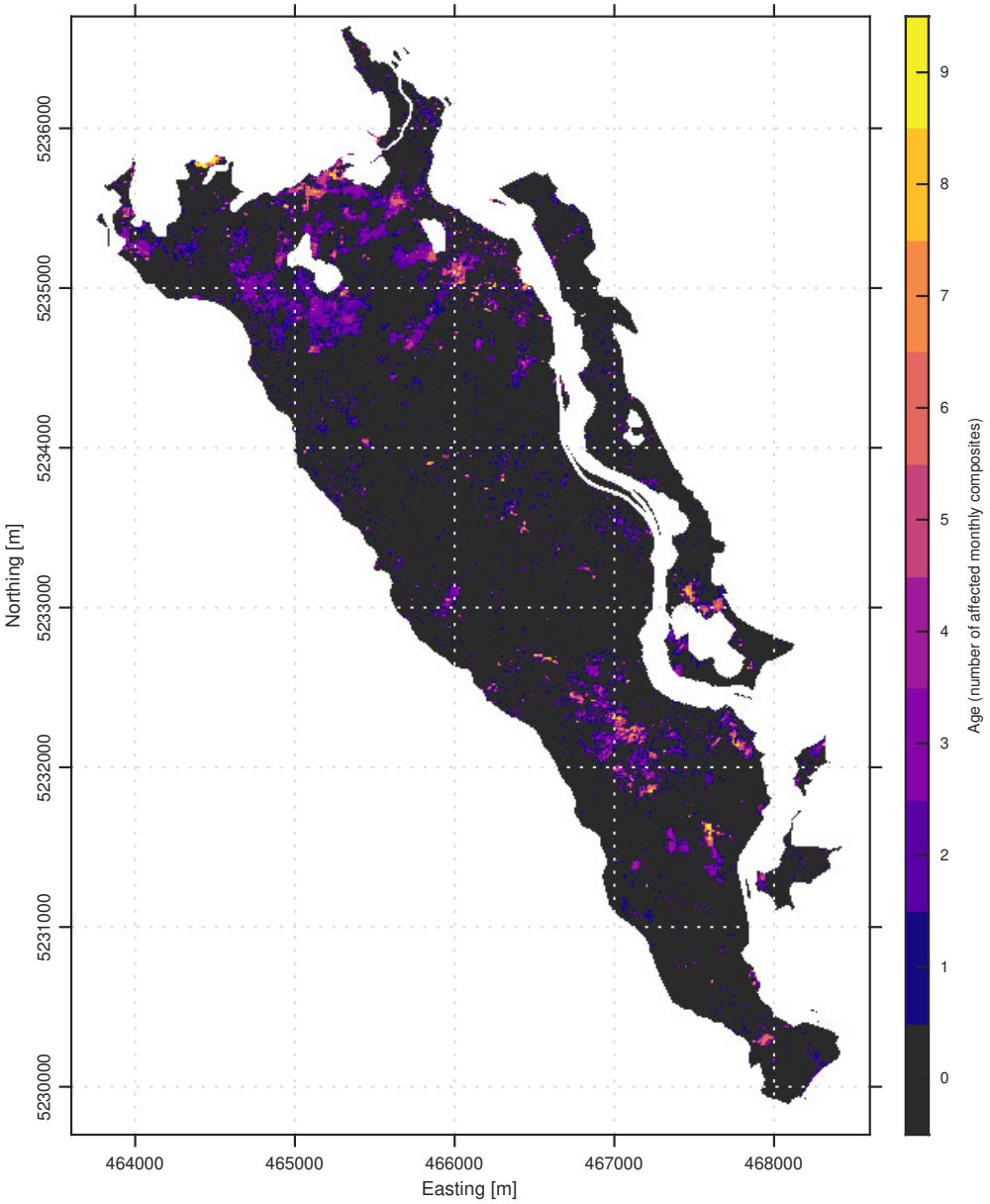

(a) Age map. Coordinates in WGS 84 / UTM zone 32N, UoM: m.

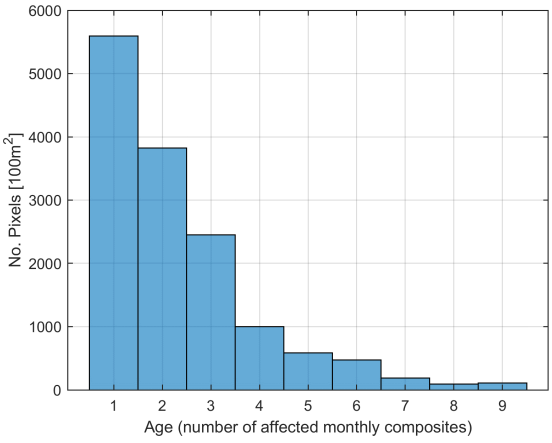

(b) Histogram of Age map.

Figure 3.2: Age product.

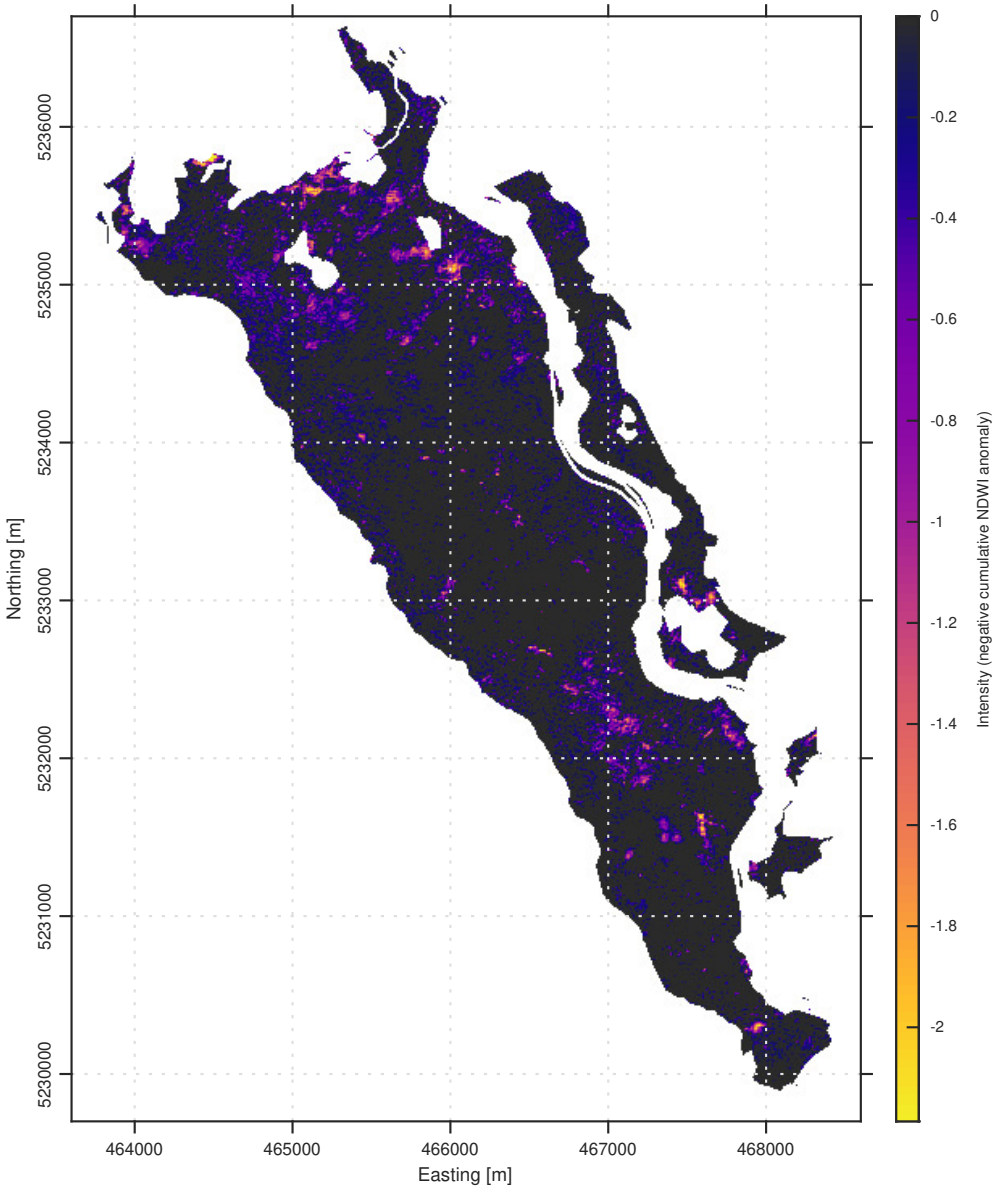

(a) Intensity map. Coordinates in WGS 84 / UTM zone 32N, UoM: m.

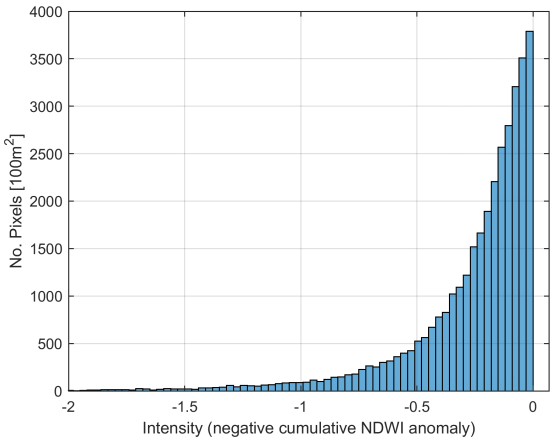

(b) Histogram of Intensity map.

Figure 3.3: Intensity product.

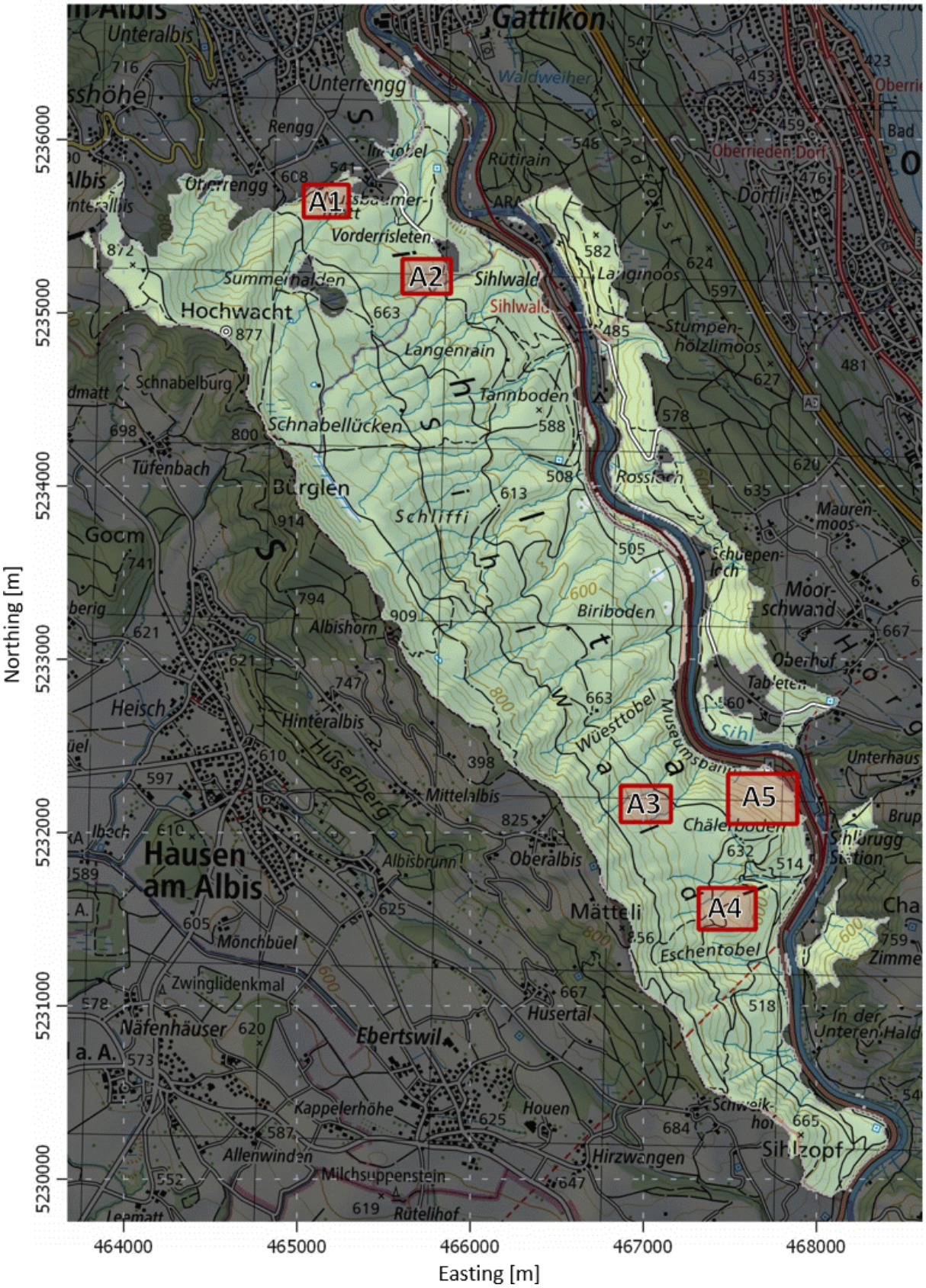

Figure 3.4: Overview Map over the close up positions for the pixel-based results. Coordinates in WGS 84 / UTM zone 32N, UoM: m. The background map is the Swiss Map Raster 50 from swisstopo (2018b).

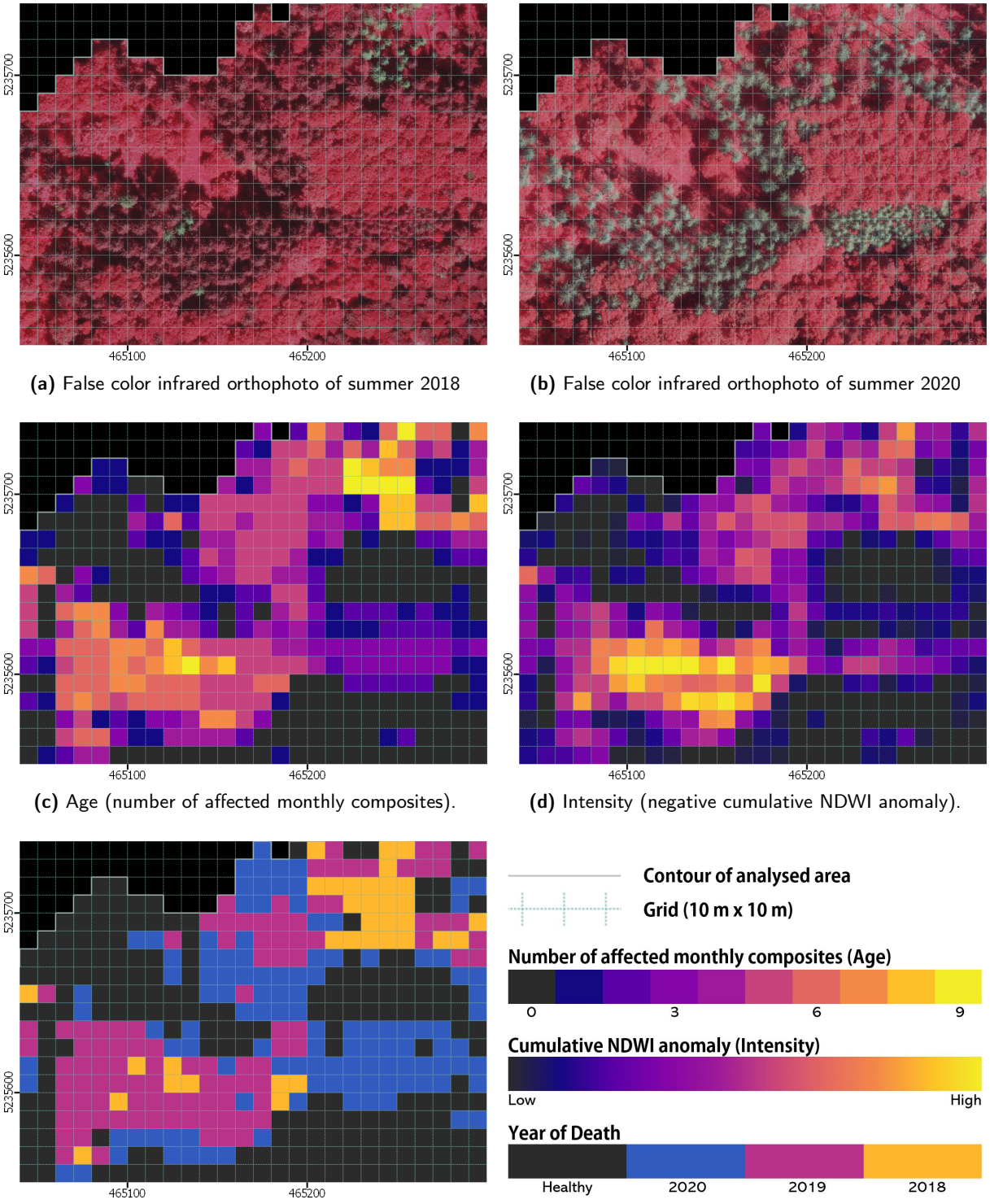

(a) False color infrared orthophoto of summer 2018

(b) False color infrared orthophoto of summer 2020

(c) Age (number of affected monthly composites).

(d) Intensity (negative cumulative NDWI anomaly).

(e) Year of Death (YOD) product.

(f) Legend.

Figure 3.5: Area 1 (A1): Close up visualisation of the results located west of *Tobel* (field name from swisstopo (2020)) within 465'040 - 465'300 East and 5'235'550 - 5'235'740 North (WGS 84 / UTM zone 32N, UoM: m). Easting is aligned along the x-Axis, northing along the y-axis. The orthophotos depicted in subplot a) and b) are provided by the Kanton Zürich (2018a, 2020).

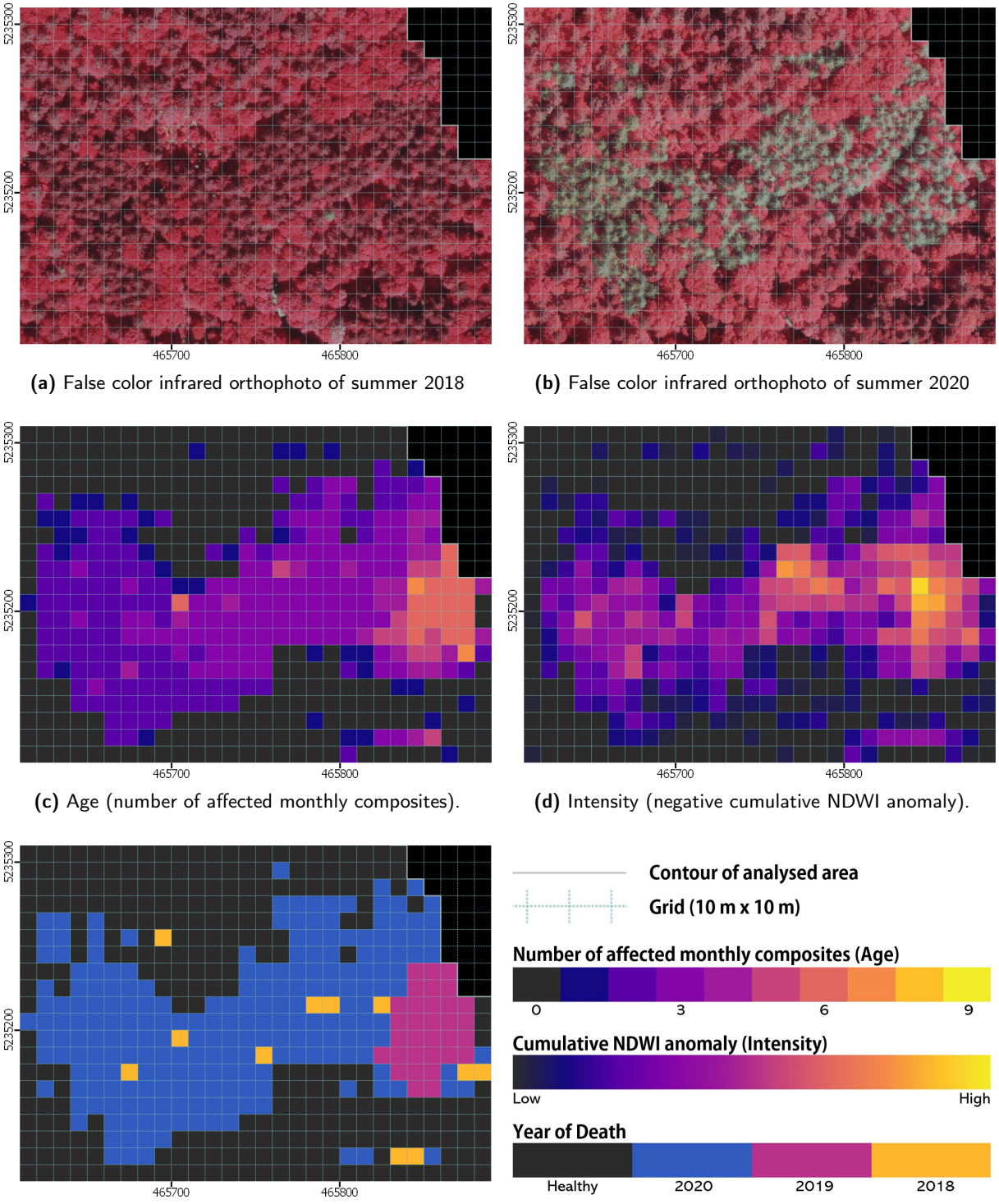

(a) False color infrared orthophoto of summer 2018

(b) False color infrared orthophoto of summer 2020

(c) Age (number of affected monthly composites).

(d) Intensity (negative cumulative NDWI anomaly).

(e) Year of Death (YOD) product.

(f) Legend.

Figure 3.6: Area 2 (A2): Close up visualisation of the results close to *Cholbenholz* (field name from swisstopo (2020)) within 465'610 - 465'890 East and 5'235'110 - 5'235'310 North (WGS 84 / UTM zone 32N, UoM: m). Easting is aligned along the x-Axis, northing along the y-axis. The orthophotos depicted in subplot a) and b) are provided by the Kanton Zürich (2018a, 2020).

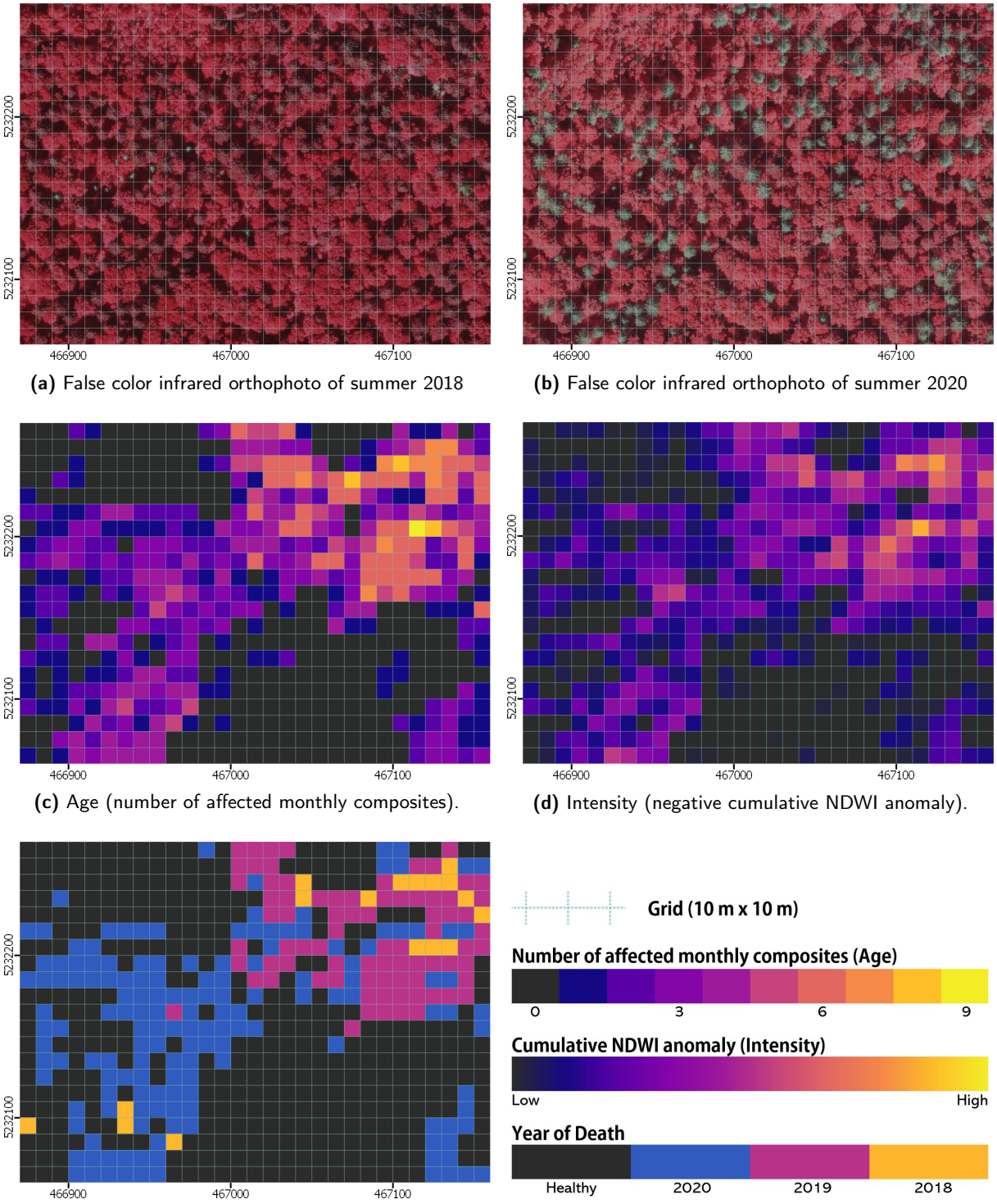

(a) False color infrared orthophoto of summer 2018

(b) False color infrared orthophoto of summer 2020

(c) Age (number of affected monthly composites).

(d) Intensity (negative cumulative NDWI anomaly).

(e) Year of Death (YOD) product.

(f) Legend.

Figure 3.7: Area 3 (A3): Close up visualisation of the results in between *Egliboden* and *Im roten Meer* (field names from swisstopo (2020)) within 466'870 - 467'160 East and 5'232'060 - 5'232'270 North (WGS 84 / UTM zone 32N, UoM: m). Easting is aligned along the x-Axis, northing along the y-axis. The orthophotos depicted in subplot a) and b) are provided by the Kanton Zürich (2018a, 2020).

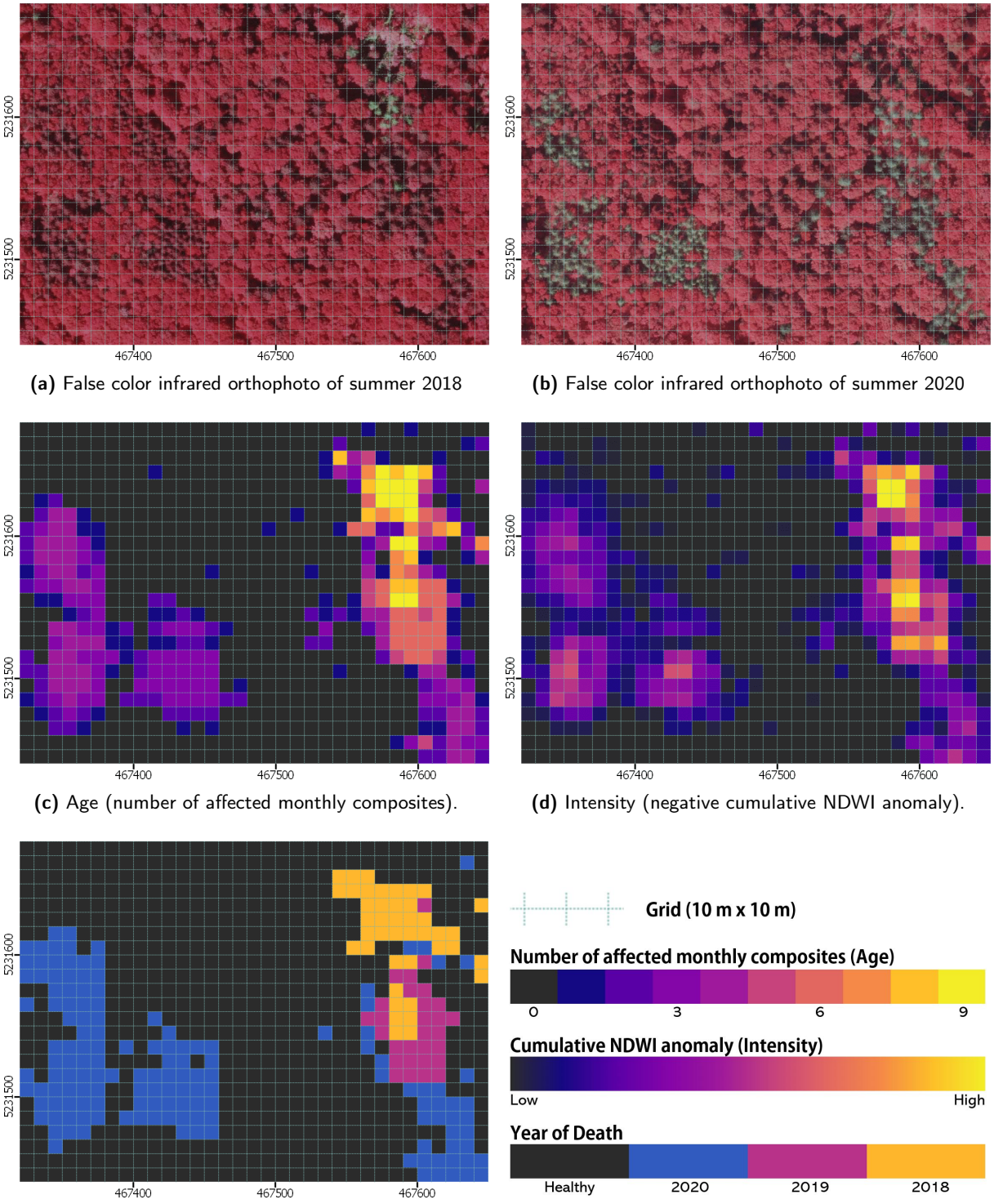

(a) False color infrared orthophoto of summer 2018

(b) False color infrared orthophoto of summer 2020

(c) Age (number of affected monthly composites).

(d) Intensity (negative cumulative NDWI anomaly).

(e) Year of Death (YOD) product.

(f) Legend.

Figure 3.8: Area 4 (A4): Close up visualisation of the results close to *Schönboden* (field name from swisstopo (2020)) within 467'320 - 467'650 East and 5'231'440 - 5'231'680 North (WGS 84 / UTM zone 32N, UoM: m). Easting is aligned along the x-Axis, northing along the y-axis. The orthophotos depicted in subplot a) and b) are provided by the Kanton Zürich (2018a, 2020).

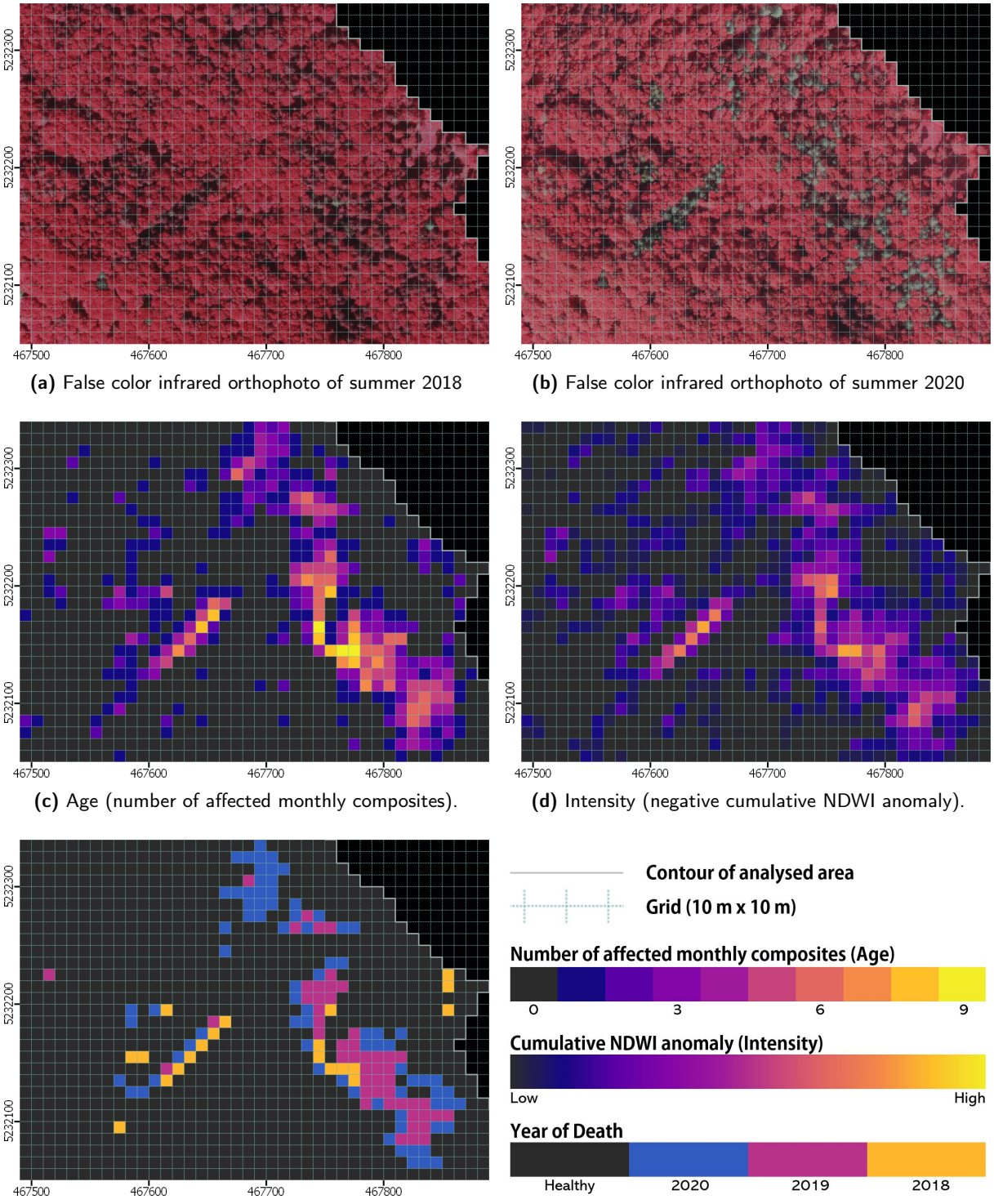

(a) False color infrared orthophoto of summer 2018

(b) False color infrared orthophoto of summer 2020

(c) Age (number of affected monthly composites).

(d) Intensity (negative cumulative NDWI anomaly).

(e) Year of Death (YOD) product.

(f) Legend.

Figure 3.9: Area 5 (A5): Close up visualisation of the results close to *Bruggrain* (field name from swisstopo (2020)) within 467'490 - 467'890 East and 5'232'050 - 5'232'340 North (WGS 84 / UTM zone 32N, UoM: m). Easting is aligned along the x-Axis, northing along the y-axis. The orthophotos depicted in subplot a) and b) are provided by the Kanton Zürich (2018a, 2020).

Figure 3.10: Forest area in the southern part of *Sihlwald*, corresponding to Area 5. The photo was taken on 14.08.2019 from 468'192 E, 5'232'690 N (coordinates in WGS 84 / UTM 32N) facing south-west by Emanuel Uhlmann.

3.2 Patch-based Approach

3.2.1 Patch Definition

One method to further investigate the dispersal patterns of bark beetles is to define interconnected regions of affected pixels, which are, from now on, referred to as patches. The adopted procedure allows a retrospective insight into the temporal development of each patch. The definition of the patches is based upon the most recent monthly NDWI diffToRef composite (August 2020 - August 2017), as illustrated in Fig. 3.11a. Brown colors represent areas which have become dryer since 2017 while green colours exhibit areas with an increased humidity compared to the reference year. This product is thresholded as described in Section 2.4.2, thus resulting in a Boolean map that distinguishes between healthy pixels (white) and affected pixels (black) (Fig. 3.11b). Thereafter, a morphological opening as described in Section 2.3.1 is applied to the affected-pixel mask, with the purpose of grouping contiguous affected pixels into the same patch (Fig. 3.11c). The parameters used for thresholding and morphological opening are detailed in Tab. 3.1. Lastly, each connected region is assigned a unique identifier, enabling the separate monitoring of the patches, as shown in Fig. 3.11d.

Table 3.1: Parameters used for the patch definition.

	Thresholding		**Erosion**		**Dilation**	
	Band	Value	Radius [m]	Iterations	Radius [m]	Iterations
Patch definition	NDWI diffToRef	<-0.09	10	1	10	1

3.2.2 Patch-based Products

After the patch definition described above, the monthly NDWI diffToRef composites were exploited in order to assess how the state of each of the resulting patches changes over time. More specifically, two different features were extracted for each month of the analysis time frame. These features are the Historical Size (HistSize) and the Historical Intensity (HistIntensity).

HistSize: The HistSize measure quantifies the growth development over time. It is calculated as follows: within each patch, and per monthly composite, the number of pixels falling below the threshold described in Section 2.4.2, are summed up.

HistIntensity: HistIntensity measures the quantitative development of the monthly NDWI diffToRef values for the patch of interest. For each monthly composite, the mean NDWI diffToRef value is computed. The choice of the mean over the median is justified by the fact that the former is more sensitive to outliers or extreme values.

3.2.3 Patch Results

The results for five of the largest patches are summarized in Fig. 3.12. Fig. 3.12a gives an overview over the positions of the patches of interest, which are all located in the northern part of *Sihlwald*. It is worth mentioning that these are not the only patches that were identified by the proposed algorithm; nonetheless, the remaining ones, which are colored in light gray in Fig. 3.12a, are not discussed herein. Moreover, it should be noted that there exists a direct connection between two of the patches (i.e., Patch 1 and Patch 2), and two of the excerpts discussed in Section 3.1. In fact, Patch 1 and Patch 2 are contained in Area 1 and Area 2, respectively.
The temporal development within the patches is shown in Fig. 3.12b and Fig. 3.12c. The former depicts the temporal variation of the number of affected pixels per patch, from now on referred to as HistSize. What all patches have in common is the fact that this number increases over time and flattens during the last two months. It is possible to recognize two main trends in Fig. 3.12b: Patch 1 and 5 react earlier, and exhibit the most prominent differences during summer 2019. On the other hand, the remaining patches present smoother behaviours until end of summer 2019, and they exhibit abrupt discontinuities in early summer 2020.

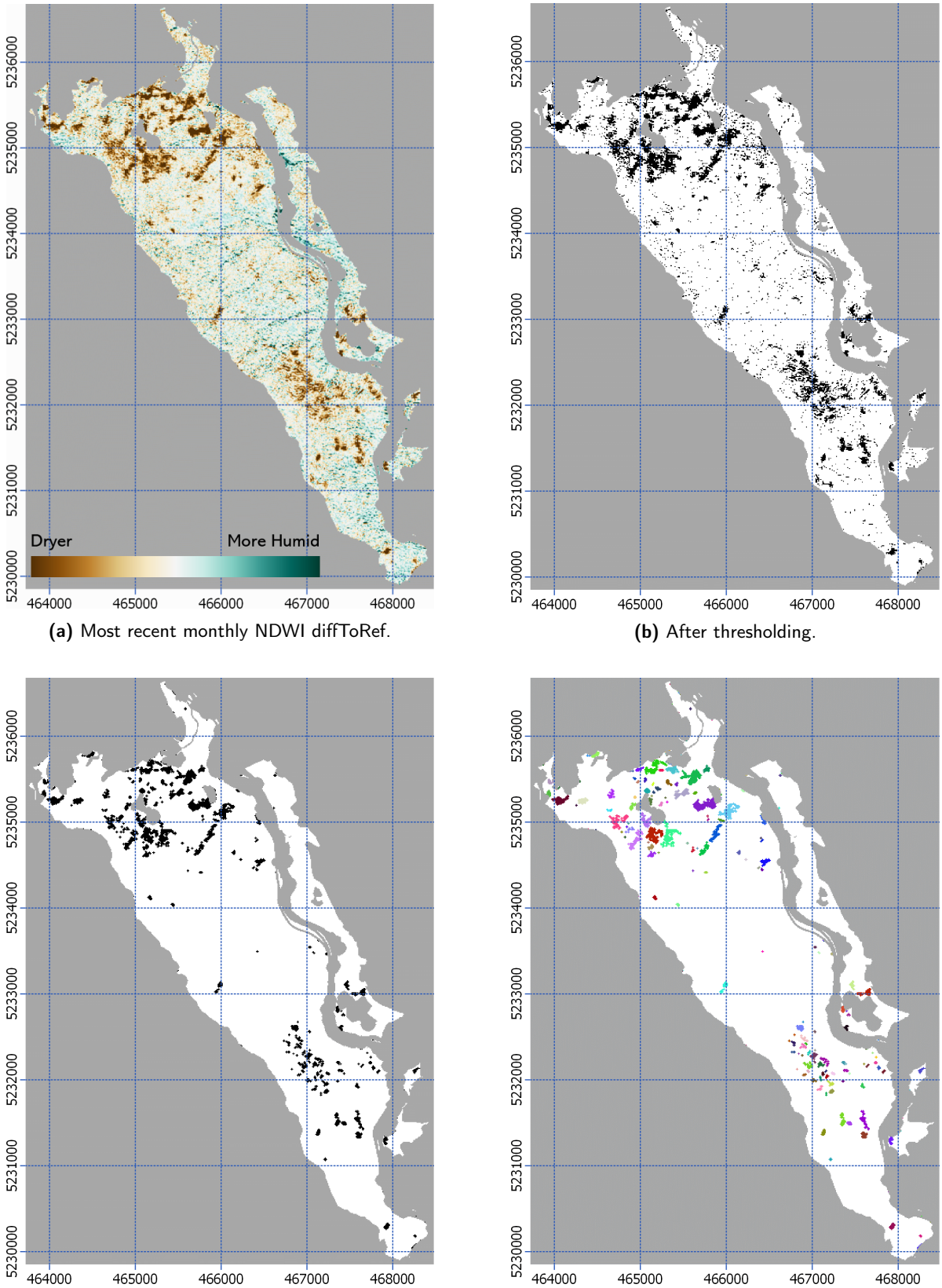

(a) Most recent monthly NDWI diffToRef.

(b) After thresholding.

(c) After morphological opening.

(d) Resulting patches.

Figure 3.11: Overview of the patch definition process. Coordinates in WGS 84 / UTM zone 32N, UoM: m. Easting is aligned along the x-Axis, northing along the y-axis.

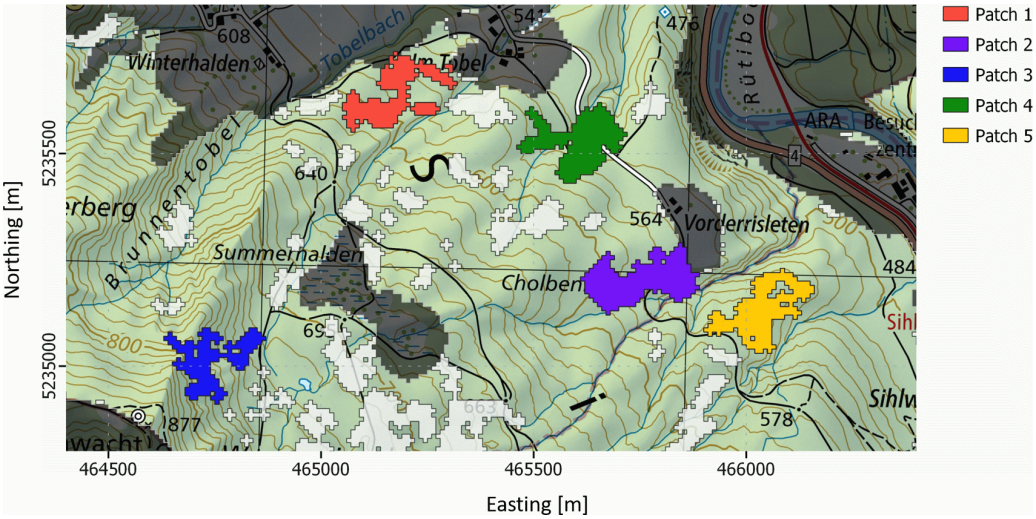

(a) Overview Map in the northern part of *Sihlwald* over the positions of five of the biggest patches. Coordinates in WGS 84 / UTM zone 32N, UoM: m. The background map is the Swiss Map Raster 25 from swisstopo (2018a).

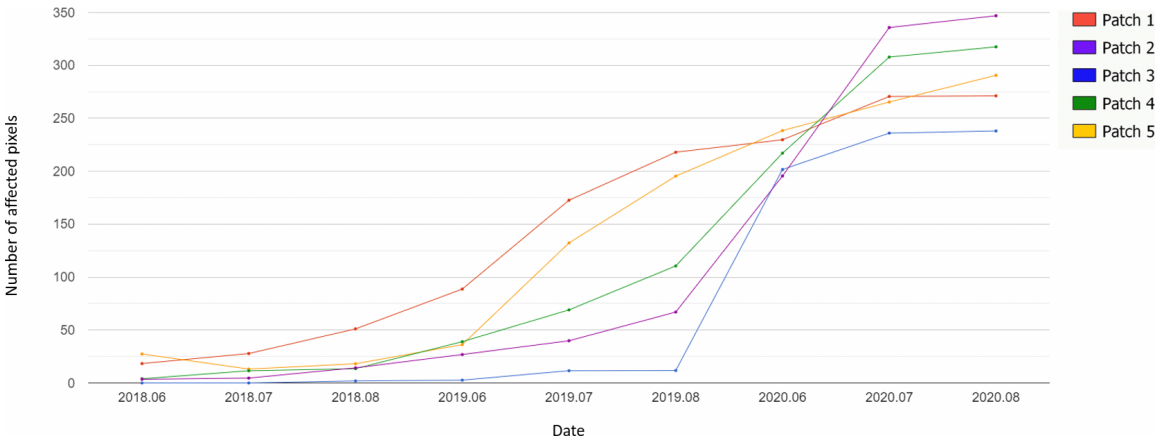

(b) HistSize: Number of affected pixels over time.

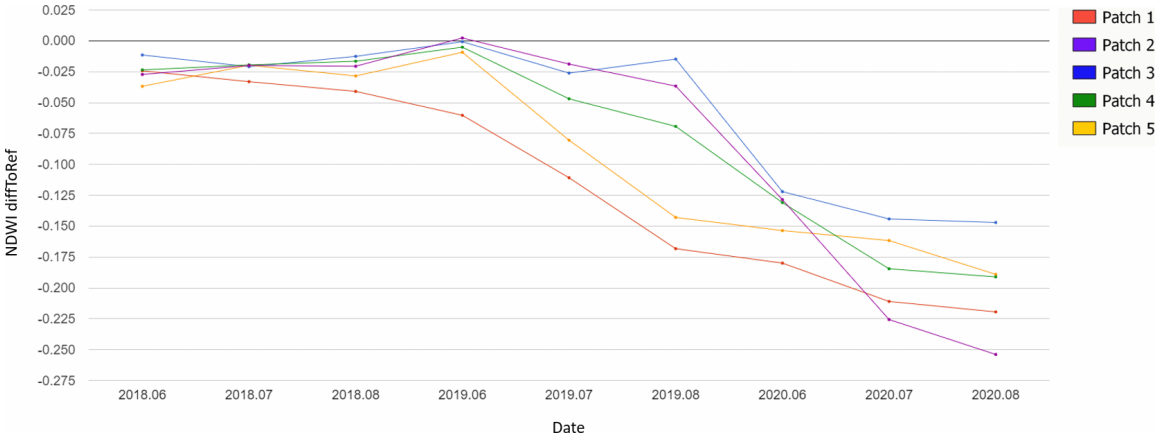

(c) HistIntensity: NDWI diffToRef values over time.

Figure 3.12: Overview and temporal development for five of the largest patches.

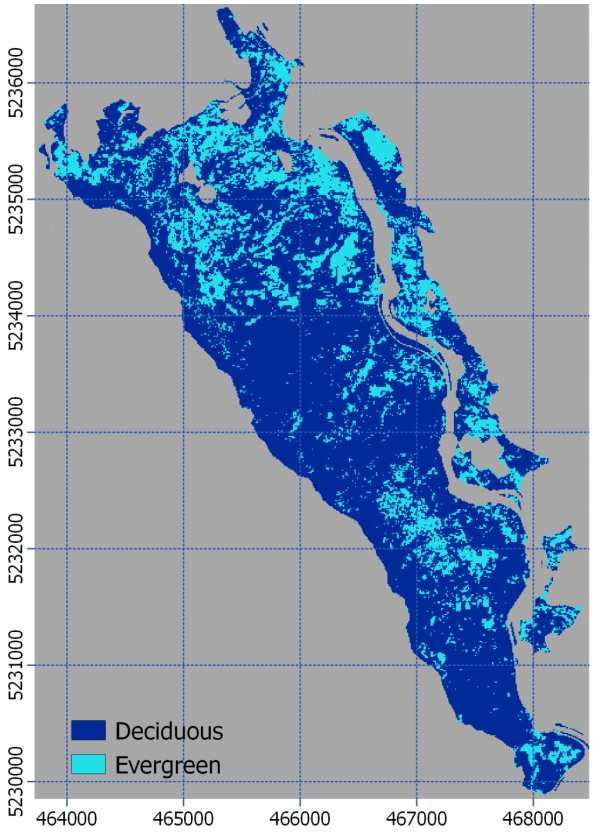

Figure 3.13: Map distinguishing in between evergreen and deciduous areas. Coordinates WGS 84 / UTM zone 32N, UoM: m. Easting is aligned along the x-Axis, northing along the y-axis.

Fig. 3.12c illustrates the HistIntensity values over time. From a simple visual analysis, it can be inferred that, for each patch, the trend decreases over time. Positive increments are rare, short-term and very moderate. The behaviour of the five patches is rather similar in the first three time samples (i.e., summer 2018) and in the last two: in fact, the values change only slightly. The main differences can be seen between August 2018 and June 2020, and, on the basis of the patches behaviours, we can define two different groups. Patch 1 and Patch 5 exhibit abrupt changes since early summer 2019, and the corresponding curves appear to flatten as of end of summer 2019. Vice-versa, the behaviour of the remaining patches is somehow delayed: even though they also start decreasing in early summer 2019, the most prominent differences are experienced between end of summer 2019 and beginner of summer 2020.

3.3 Numerical Evaluation

The diffSuWi product was further processed in order to discriminate the ROI pixels between evergreen and deciduous. This was performed by comparing the diffSuWi values with an appropriate threshold. The latter is defined on the basis of the intersection point between the estimated distributions of the two variables, as described in Section 2.5. The resulting output,

Table 3.2: Values of the numerical Evaluation.

[%]	**Pixel-based**	**Patch-based**
Affected Area in ROI	10.56	5.54
Non-affected Area in ROI	89.44	94.46
Evergreen in Affected Area	61.30	76.66
Deciduous in Affected Area	38.70	23.34
Affected Area in Evergreen	25.97	17.04
Affected Area in Deciduous	5.45	1.72

which is depicted in Fig. 3.13, is a Boolean map which exhibits the spatial distribution of the two afore-mentioned classes. The estimated evergreen and deciduous ratios constitute the 24.94 % and 75.06 %, respectively, of the overall ROI.

The derived detections were used in order to quantify the relative dimension of the affected areas with respect to the overall ROI, thus yielding the *Affected Area in ROI*. Moreover, additional measures were computed. The *Evergreen (Deciduous) in Affected Area* quantifies the ratio of evergreen (deciduous) pixels within the affected areas. Vice-versa, the *Affected Area in Evergreen (Deciduous)* quantifies the ratio of unhealthy pixels within the evergreen (deciduous) areas. All the afore-mentioned measures were computed by taking into consideration the two available products (i.e., the pixel- and patch-based product). The affected pixels were defined based on two different masks: the pixel-based mask is the thresholded, most recent monthly diffToRef composite (Section 3.2.1), constituting the baseline product to define the patches. The patch-based mask is built on the pixel-based one; nonetheless through morphological operations single and small-sized detections are removed, as described in Section 3.2.1. Therefore, the patch-based mask exhibits only the larger affected areas. The resulting values are summarized in Tab. 3.2: for the patch-based case, the *Affected Area in ROI* results to be roughly half that of the pixel-based case. Furthermore, when switching from pixel- to patch-based, the *Evergreen in Affected Area* value substantially increases.

4 Discussion

4.1 Product Overview

Table 4.1: Summary of the products and the their information content.

		YOD	Age	Intensity	HistSize	HistIntensity
PRODUCT CHARACTERISTICS	**Product format**	map	map	map	graph	graph
	Pixel- / patch-based	pixel-based	pixel-based	pixel-based	patch-based	patch-based
	Thresholding applied	yes	yes	no	yes	no
	Temporal resolution	yearly	monthly	monthly	monthly	monthly
TIME	**Start**	✓	∼		✓	✓
	Duration		✓		✓	✓
	Temporal development	✓	✓		✓	✓
SPACE	**Location**	✓	✓	✓	∼	∼
	Spatial context	✓	✓	✓		
QUANTIFICATION	**Intensity**			✓		✓
	Size	∼	∼	∼	✓	

Table 4.1 showcases an overview over the available products, and it summarizes their main characteristics. Furthermore, it emphasizes the information content of a given product. The *TIME* category is subdivided into the three main temporal features, which are listed as follows. The feature *Start* refers to the time stamp at which an area is affected for the first time, whereas *Duration* refers to how long the process has lasted. Furthermore, the feature *Temporal development* informs on how the state of the area of interest has changed over time. Similar considerations can also be made for the spatial information. The *SPACE* features clarify whether the coordinates of a given area are included in the product (*Location*), and whether the spatial context is apparent (*Spatial context*). Lastly, the two features in the *QUANTIFICATION* Section express whether the product of interest exhibits how severely an area has degraded over time (*Intensity*), and how large the area is (*Size*). The check-mark sign (✓) indicates that a product directly informs about a given measure. The tilde sign (∼) indicates partial, indirect or qualitative information, whereas an empty field indicates that such a question cannot be answered by the product.

The pixel-based maps (i.e., YOD, Age and Intensity) summarize the changes over the observation time frame in one product. They give an overview over the processes in the whole forest and inform about the spatial context. The patch-based products (i.e., HistSize and HistIntensity) allow a more detailed insight into the emergence and temporal development of a specific region.

YOD: The YOD map is the most simplified result of this study: it is a yearly product and it marks a pixel as affected if the NDWI diffToRef of the yearly composite falls below the threshold. Flagged pixels are no longer considered in the following years, thus making the proposed algorithm not capable of detecting recoveries (i.e., vegetation becoming healthier). The product gives a first, rough overview over the temporal development of the spread of bark beetles in *Sihlwald*.

Age: The Age map is computed on the basis of the thresholded monthly composites. While it could be described as a similar product to the YOD map, though having a better temporal resolution, its information content is slightly different. The Age value related to a given pixel quantifies how many times this pixel has been detected as unhealthy. Nevertheless, it does not necessarily inform about the exact date, which is clearly given only with the highest value of the map (i.e., 9). Notwithstanding, under the assumption of bark beetles causing increasing damage over time, and that the affected trees have not recovered, Age values result to be directly linked to the start time of the infestation.

Intensity: The Intensity values are derived from the monthly composites, and they do not undergo any thresholding approach. Such product informs on the severity of the ongoing processes by providing a cumulative measure. The latter can take on either positive or negative values, which identifies areas that got healthier or unhealthier, respectively. As this thesis mainly focuses on the impact of bark beetles on spruce trees, and in light of the fact that affected trees likely exhibit a deteriorated health status, only negative cumulative measures are considered in the Intensity measure.

HistSize: The HistSize measure provides information about the growth development per patch. This measure does not exhibit any spatial information, that is it cannot express how the shape of the affected area changes over time.

HistIntensity: HistIntensity informs about the quantitative development of the monthly NDWI diffToRef values per patch. This is particularly useful, especially when only few pixels within the patch are affected. Hence, the derived measure informs about the development of the average health state. Nevertheless, the derived signal is very dependent on the size of the defined patch. Let us assume that there are five affected pixels in a patch of 300 pixels. The impact of the affected area on the average NDWI diffToRef value is substantially smaller than in a patch of 50 pixels. Thus, the comparison of patches with very diverse sizes has to be handled carefully.

Comparison of Age and Intensity: The Age map and the Intensity map give a visually similar impression. The correlation between Intensity values and Age values is made explicit in Fig. 4.1. As depicted in the scatter plot of Fig. 4.1a, pixels with moderate Intensity values (i.e., > -1) and low Age values (i.e., < 3) are the most frequent ones. An additional scatter plot, the one in Fig. 4.1b, emphasizes the correlation between the two variables: the red line, the linear relation that best fits the two measures, exhibits a determination coefficient (R^2) of 0.71. Although there is a strong negative correlation of the two measures, they can vary in certain cases.

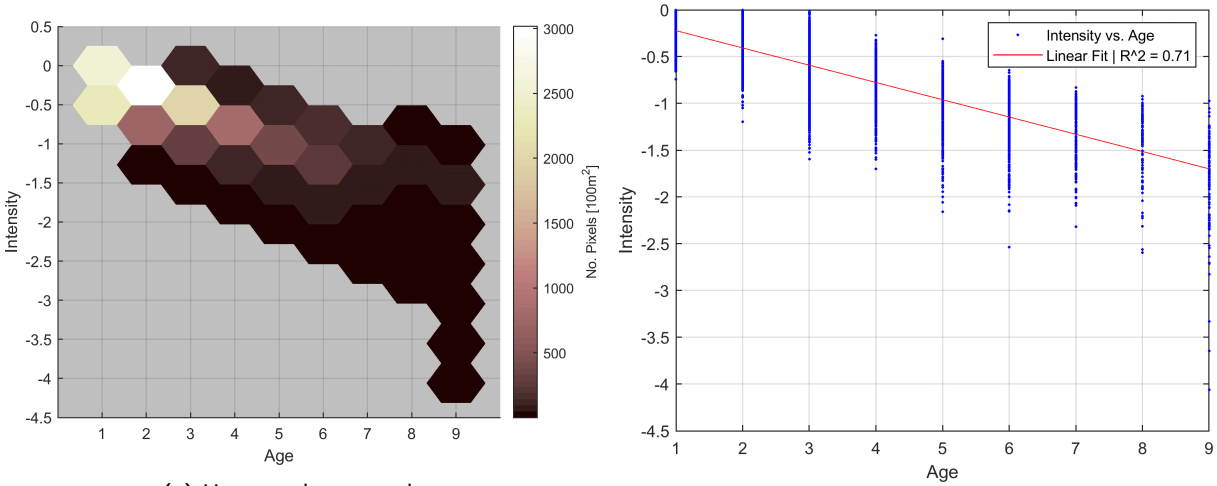

(a) Hexagonal scatter plot.

(b) Linear fit.

Figure 4.1: Comparison and correlation in between Age and Intensity values.

4.2 Algorithm Performances

Qualitative Analysis: The performances of the algorithm have been assessed by comparing the derived products with high resolution aerial images (Kanton Zürich, 2018a, 2020). While this is not an in-depth numerical validation, yet, it is a first step to evaluate whether the derived products are reliable or not.

In Area 1 (Fig. 3.5), some of the trees in the upper right corner of the excerpt appear to be unhealthy already in summer 2018, as depicted in Fig 3.5a. This feature is preserved in the obtained products: in fact, both Age and YOD map exhibit high values in the corresponding region, thus indicating that these pixels were detected as unhealthy in 2018. As the algorithm takes the imagery of 2017 as reference, the high values in the aforementioned region indicate that the trees health has decreased in 2018. Moreover, in the right-hand side of Fig. 3.5b, it is possible to see that the affected area presents a circular contour, and that the area within this circle appears to be healthy. The very same features are evident from Fig. 3.5c to Fig. 3.5e: in fact, for the area within the aforementioned circle, Age and YOD values are 0, whereas the Intensity values are close to 0.

Although there is an overall strong negative correlation between Age and Intensity, their values can differ under specific conditions. In this regard, Area 1 results to be a meaningful example. In fact, while for Age and YOD the highest values are located top-right, Intensity shows a cluster with high values in the bottom-left quadrant. This difference is likely caused by the density of affected trees. The more dense the population of affected trees in a given pixel, the lower the NDWI diffToRef value with respect to the monthly composite. This influences the Intensity product more strongly, as the actual NDWI diffToRef values are accumulated. This is not the case for the Age product: in fact, once the NDWI diffToRef value is below the threshold for a given monthly composite, it does not play a role any longer. In light of the above, areas with relatively higher Intensity values and, at the same time, moderate Age values, suggest a dense

population of affected trees. On the other hand, relatively higher Age values, in combination with moderate Intensity values, are likely caused by areas with a rather scarce population of affected trees.

Moreover, it is worth highlighting that the details of the aerial images are much better than that of the obtained products. This is not caused by the algorithm itself, but it is a consequence of the spatial resolution of the input data-sets.

The HistSize and HistIntensity plots describe the temporal variation of size and severity of the ongoing process in the affected area. For instance, in Patch 1 (Fig. 3.12b), the progression of the HistSize increases in a more gradual fashion compared to the other patches which have a later onset of growth. The graph, therefore, suggests a larger amount of pixels with high Age values in Patch 1 (corresponding to Area 1), with respect to Patch 2 (corresponding to Area 2). A comparison with Fig. 3.5 and Fig. 3.6, respectively, facilitates this observation.

The results for Area 2 (Fig. 3.6) suggest that the 2018 detections might have triggered the subsequent spread pattern. The yellow/orange colored pixels might have been the *seed* for the spread of bark beetles. The Age map suggests a cascade-like spread in mainly three different episodes within 2019 and 2020. The high Intensity values are likely produced by a greater density of affected trees, which is confirmed by the 2020 orthophoto (Fig. 3.6b), with relatively high Age values (i.e., a long lasting spread pattern). The afore-mentioned findings correspond well with the patch-based results of Patch 2, depicted in Fig. 3.12. The main growth and drop in HistSize and HistIntensity, respectively, happen after August 2019.

Area 3, whose results are depicted in in Fig. 3.7, was chosen to evaluate the algorithm capabilities to reflect changes in an area with a rather scarce distribution of affected trees. The scatter pattern of the affected trees in the 2020 orthophoto is preserved in all three resulting maps. The Age and YOD map suggest a gradual spread over time, progressing from top right to bottom left.

A fairly homogeneously colored and sharp-edged accumulation of pixels in the top-right corner of the Age map of Area 4 (Fig. 3.8c) suggests a rather radical and fast happening event. The bright yellow colour indicates that the change from healthy vegetation to impaired vegetation has happened between summer 2017 and summer 2018. Zooming into the 2018 orthophoto (Fig. 3.8a) reveals lying trees in the depicted area. Likely, these damages were produced by the storm Burglind/Eleanor in January 2018 (MeteoSwiss, 2018a).

The photography in Fig. 3.10 depicts affected trees in a peculiar line running from from north-east to south-west. The produced maps in the corresponding area replicate this feature rather neatly (Fig. 3.9).

In light of the above, it is clear that the proposed algorithm replicates most of the spatial and temporal features of the spread patterns. Nonetheless, some differences between the derived results and the available orthophotos exist. Possible explanations are given as follows. When overlaying the derived maps with the corresponding orthophotos, sometimes, it appears as if the two images were not perfectly co-registered. This effect can be caused by the looking angle of the orthophotos, which are co-registered based on the surface of the mapped area. A change in looking angle can cause a shift of the visualisation of the tree crown of up to roughly 10 m. Furthermore, in certain cases, affected trees are visible in the orthophoto, but they are not present

in the results. Possible reasons for the omission of affected areas are as follows. When a single unhealthy tree is surrounded by healthy vegetation and, at the very same time, it is located in the crossing point of four pixels, its contribution in terms of NDWI might not be large enough to flag the four pixels as affected. Moreover, this could also be explained by the fact the these trees had been affected already as early as in the reference year. In such a case, the corresponding area will have a rather small decrease in NDWI in the following years, thus resulting in NDWI diffToRef values close to zero, and, hence, no detections.
Another difference between the obtained results and the orthophotos is represented by those pixels that are mapped as affected, although this is not confirmed by the 2020 orthophoto. One possible reason for this is the discrepancy between the end of the analysis time-frame and the orthophoto acquisition time. The area of interest might have become brown after the 10-th of August. Another possibility is the sensitivity of NDWI to the green-attack state of a bark beetle infection (Abdullah et al., 2019). In this case, an area could be mapped as affected before the change becomes apparent in a false color orthophoto.

Numerical Evaluation: The ratio of affected pixels in the ROI (i.e., Affected Area in ROI) results to be 10.56 % and 5.54 % when using the pixel- and the patch-based approach, respectively, as summarized in Tab. 3.2. Since no detailed quantitative set of ground data is available, such values cannot be validated. Nevertheless, the reliability of the results can be inferred by quantifying the ratio of evergreen and deciduous in the affected areas (i.e., Evergreen/Deciduous in Affected Area). This is driven by the fact that bark beetles affect only spruce trees, which belong to the evergreen category. Therefore, if the large majority of affected pixel was classified as deciduous, this would raise a serious question about the performances of the proposed approach. The values summarized in Tab. 3.2, however, clearly state the opposite.
The relative disparity between Evergreen/Deciduous in Affected Area increases when using the patch-based approach. This is likely due to the fact that most small-scale affected areas are mapped as deciduous and, therefore, they do not contribute to the final results in the patch-based approach. Lastly, the ratio of affected area within evergreen regions (i.e., Affected Area in Evergreen) is significantly larger than in deciduous areas (i.e., Affected Area in Deciduous). These values concur with a bark beetle spread occurring only in evergreen areas.

4.3 Decomposition of Forest Impairment Causes

When *a-priori* knowledge or ground measurements are not available, it is not possible to evaluate whether the pixels detected as unhealthy are a direct consequence of a bark beetle infestation, or whether they are induced by other natural phenomena such as droughts, fires, storms, etc. Moreover, it is worth mentioning that the aforementioned events are often times connected with each other, and they might intervene either at the same time, or in subsequent periods. For instance, bark beetles are more likely to appear after catastrophic events that decrease the health status of vegetation and provide breeding ground for insects. What can be said for certain is that affected pixels within deciduous regions are most likely not caused by a bark beetle infestation, as these insects do not attack such trees. Furthermore, analyzing the temporal development of

a patch of interest (see, for instance, Fig. 3.12) gives an insight into the ongoing processes. In fact, the gradient of the HistSize and HistIntensity functions is expected to be smoother for a bark beetle infestation, which gradually attack trees. On the contrary, fires or storms, due to their rapidly evolving nature, would induce more abrupt features in the results.
The observation of the Age map can give an insight into the spatio-temporal development of an ongoing process. Fairly homogeneously colored and sharp-edged pixel accumulations with high Age values, such as in Area 4 (Fig. 3.8), suggest the influence of rather drastic events. On the basis of the derived high Age values, which refers to an event happened between summer 2017 and summer 2018, a possible explanation is that the effects in this area are a direct consequence of the January 2018 Burglind/Eleanor storm (MeteoSwiss, 2018a).

4.4 Methodology

4.4.1 Cloud Filtering

Despite the simplicity of the cloud filtering approach, its effectiveness in forested areas is of satisfactory nature. Due to the implemented approach, very small clouds and their shadows (i.e., $< 5\,\text{m} \times 5\,\text{m}$) are the main reason for omission error, while larger areas (i.e., $> 5\,\text{m} \times 5\,\text{m}$) in shaded slopes contribute to the commission error of the cloud mask. Furthermore, it is worth mentioning that, although the described approach is successful for forested areas, the performance score is far below a workable standard for most other surfaces such as houses or streets, bare soil, crops, and water bodies (Fig. 2.3c). As an alternative to the implemented approach, authors such as Frantz et al. (2018), Schmitt et al. (2019), Singh and Komodakis (2018) and Skakun et al. (2017) have suggested sophisticated approaches to filter cloud influences for all surface types.

4.4.2 Reference

The results presented herein were obtained by using the year 2017 as reference. As explained in Section 2.2.2, this year precedes the major spread of bark beetles. Furthermore, this choice was also influenced by data availability: that is, Sentinel-2 Level-2A data are available since March 2017 in the GEE data catalog (Gorelick et al., 2017). A reference consisting of several years of imagery would have have been more stable and, likely, it would have led to less data fluctuations. Furthermore, when using the year 2017 as reference, changes occurred in earlier years cannot be mapped.

4.4.3 Thresholding

Affected vs. Healthy Regions: When looking at the histogram of the YOD values (Fig. 3.1b), it is clear that there exists a huge disparity between the 2020 detections and the ones from the previous years. In other words, the large majority of pixels was detected for the first time in the year 2020. In order to better understand whether these values are reliable or not, the input data were analyzed from a statistical perspective. Fig. 4.2 shows the box plot obtained from the NDWI diffToRef values for the years of the analysis time frame. It is worth mentioning that the

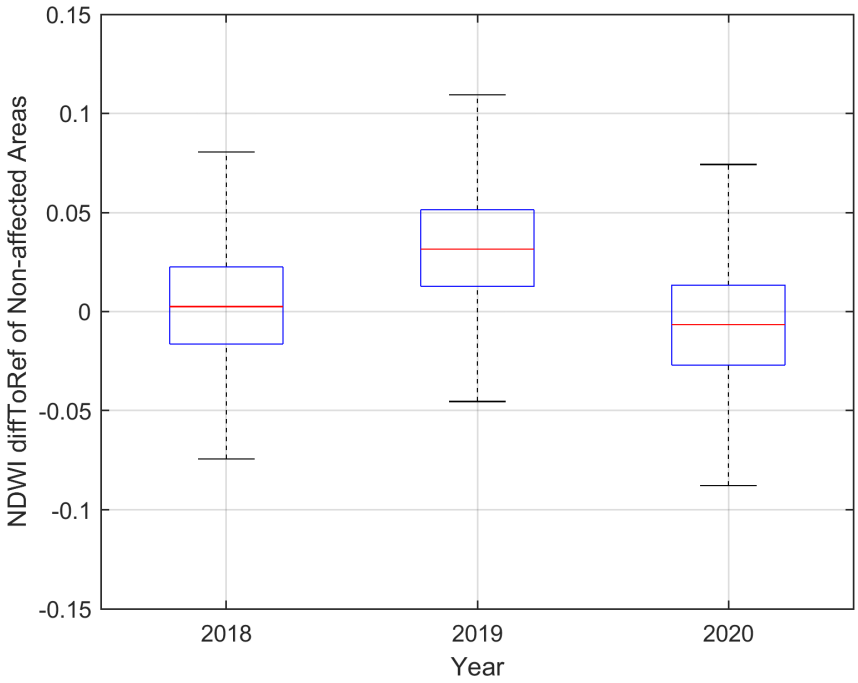

Figure 4.2: Boxplots showing the NDWI diffToRef values of non-affected pixels over the years 2018 - 2020.

affected pixels were excluded from the analysis, and that the resulting box plot is based only on the healthy pixels. The box plot can be explained as follows: the median values of the three data-sets are represented by the red lines. Moreover, the lower and upper boundary of each box are defined by the 25-th (i.e., q_1) and 75-th (i.e., q_3) percentiles, respectively. The black whiskers define the interval within which values are not considered outliers: a value is classified as an outlier if it is greater than $q_3 + (q_3 - q_1)$ or smaller than $q_1 - (q_3 - q_1)$. Outliers are not displayed in Fig. 4.2.

The median values result to be substantially different: in fact, the maximum and minimum median are obtained for year 2019 and 2020, respectively. Moreover, it should be noted that q_1 for year 2019 is approximately equal to q_3 for year 2020. That is, the 50 % of the population delimited between the corresponding q_1 and q_3 values substantially differs from 2019 to 2020. A possible cause for the change in NDWI diffToRef values in non-affected areas over the years can be found in meteorological data. While all years between 2017 and 2020 had very warm and dry summers, 2018 and 2020 reached record temperatures (MeteoSwiss, 2018c,d, 2019a,b, 2020a,b, 2021b). Additionally, 2020 had a very warm spring with an ongoing dry period (MeteoSwiss, 2021b). A very warm summer was also experienced in the year 2019; nonetheless, unlike 2018 and 2020, it was much closer to the climate normals. The more moderate temperatures of 2019, in combination with more water availability, provided a more beneficial environment for trees compared to the other years. The lack of water in summer 2018 and 2020, and the additional dry spring in 2020, might have led to foliation constraints, which, in turn, translates into lower measured NDWI values.

The yearly-dependent nature of the input data-sets plays a key role in defining the amount of detections, especially in light of the fact that the proposed algorithm exploits a single global

threshold. With overall lower NDWI diffToRef values in 2019, less pixels fall below the threshold and are therefore considered affected. Compared to 2018, whose NDWI diffToRef median value is almost zero, and, therefore, similar to the reference year median, 2019 is expected to have fewer detections than 2020. In conclusion, the yearly-dependent behaviours of the input data-sets lead to an underestimation of unhealthy pixels in 2019, and to an overestimation in 2020. Although this effect is described for the yearly composites, the same issue is experienced for the monthly composites. To further improve the proposed algorithm, and to tackle the aforementioned problem, the adopted threshold shall be designed in such a way to take into consideration the intrinstic time-dependency of the input data-sets.

Evergreen vs. Deciduous: Another thresholding approach was applied in order to differentiate between evergreen and deciduous trees in the ROI (Section 2.5 and Fig. 3.13). The resulting values can be summarized as follows: the evergreen and deciduous ratio are 24.94 % and 75.06 %, respectively. These values are almost identical to the estimates derived from the 2017 *Sihlwald* sample inventory, which indicates a 25.07 % of evergreen areas (Brändli et al., 2020)).
Though the classification performances proved to be quite satisfactory, it should be noted that the classification itself is carried out on the basis of important assumptions. As described in Section 2.5, the value of the adopted threshold is inferred from the intersection point of the two functions that best fit the corresponding histograms. The proposed algorithm adopts a linear mixture model of Gaussian distributions, thus assuming that the two variables (i.e., the NDWI diffSuWi for evergreen and deciduous) are normally distributed. This model appears to fit the NDWI diffSuWi histogram with sufficient accuracy, as highlighted in Fig. 3.13; nonetheless, the veracity of the assumptions has yet to be demonstrated.

4.5 Outlook & Further Research

The spread of bark beetles has drastically reduced the amount of spruce trees in the past three years in *Sihlwald*. Assuming a similar trend in the future, the amount of spruce trees will be substantially reduced within the coming years. This is not necessarily a bad thing. In the past times, when *Sihlwald* was still a managed forest and it was used for wood production, spruce trees would thrive as they were planted and taken care of by men. Spruce trees would naturally occur only occasionally. In light of the above, it seems safe to predict that bark beetle affected areas will be replaced by secondary vegetation of other tree species, therefore bringing the forest closer to its original state (Brändli et al., 2020).
The algorithm products can be used in order to perform a spatio-temporal analysis of the affected areas. The extracted information helps us to better understand the spread patterns of bark beetle and, at the same time, it informs on the historical development in *Sihlwald*. Moreover, these products could be used in combination with other data-sets such as, for instance, a tree species inventory, in order to predict which areas are more likely to be affected. The demand for algorithms that are capable of automatically detecting and monitoring bark beetle infestations is likely to increase in the future. In fact, the current climate change scenarios increase the chances of catastrophic events (e.g., droughts, fires, etc.), from which bark beetles benefit.

The comparison and correlation of different local variables (e.g., slope, elevation, aspect, tree height, etc.) with the derived affected areas would give a deeper insight into limiting and accelerating factors of a bark beetle infestation. Additionally, a more more in-depth statistical analysis of the obtained results could reveal causal and chronological connections between environmental variables and spread patterns. Furthermore, the suggested approach could be developed to assess the correlation between increasing temperatures and the presence of bark beetles. To this end, future researches shall focus on studying meteorological parameters (e.g., rainfall, temperature, etc.) in combination with the algorithm products.

The findings of this thesis are mainly limited by two factors. The first limiting factor is that all products were computed by using a global threshold, as described in Section 4.4.3. To reduce its impact, further research shall focus on designing a monthly- and yearly-dependent thresholding approach. Such a solution would crucially reduce the impact of meteorological conditions on the detection of impaired areas. Furthermore, the proposed algorithm was designed to detect increasingly deteriorating areas, which are typical for a bark beetle infestation (Millar and Stephenson, 2015; Seidl and Rammer, 2017; Senf and Seidl, 2018). As a consequence, the algorithm is not able to recognize and map recovering regions, which are likely to develop during longer time spans. In this regard, further studies shall remove the time constraints adopted herein (i.e., the analysis time frame is limited to *only* three years). This would allow to study the long-term spatio-temporal developments of spread patterns, therefore leading to deeper insights into the mechanism of bark beetle infestations.

5 Conclusion

5.1 Summary

In this master's thesis, an algorithm for the automatic detection of bark beetle affected forest areas has been developed. The proposed algorithm exploits Sentinel-2 Level-2A BOA products in order to produce composite time-series with monthly and yearly resolution. The NDWI index is sensitive to leaf water content and was therefore utilized to map the effects of bark beetle on trees. The use of satellite data allows analyzing large areas. Compared to a laborious fieldwork, such an approach results to be much more efficient in mapping the spatio-temporal changes of the area of interest, due to its peculiar acquisition mode and revisit times. The proposed algorithm is not only able to infer the state of the forest at a specific time, but it is also capable of summarizing spatio-temporal changes for the years 2018–2020 in *Sihlwald*. Different products were designed with the primary aim to measure the characteristics of a bark beetle spread, and they were validated by using orthophotos acquired by the Kanton Zürich (2018a, 2020). The comparison between the aforementioned products and the orthophotos has demonstrated that the algorithm is capable of correctly detecting bark beetle infested areas and of mapping their spatio-temporal development.

5.2 Findings

The research questions stated in the introduction are briefly answered.

Is satellite remote sensing a suitable tool to map the dispersal of bark beetle?

The use of Sentinel-2 Level-2A BOA in combination with the NDWI index proved to be capable to detect affected areas and to differentiate them from healthy regions. Furthermore, the good temporal resolution provides a valuable baseline for a time-series analysis.

What measures are suitable to quantify and qualify the dispersal of bark beetles in *Sihlwald*?

This thesis proposes a number of products to infer the spatio-temporal characteristics of a bark beetle spread, both in qualitative and quantitative terms. Three of the products are based on a pixel-based approach and are presented as maps, summarizing the events in the analysis time frame: YOD, Age and Intensity. YOD indicates what year the pixel of interest was first recognized as dead. Age refers to the number of monthly composites a pixel was marked as affected, and Intensity reflects the cumulative change in terms of dryness. Furthermore two additional products are proposed: HistSize and HistIntensity. They are both based on a clusters of affected pixels, herein referred to as patches. Within each patch, the development of the number of affected pixels (HistSize) and the progress in terms of dryness (HistIntensity) is measured and indicated. The above mentioned products inform about spread patterns of bark beetles. The qualitative comparison of the proposed products with high-resolution airborne imagery has resulted in a good fit.

Is it possible to decompose and quantify the contribution of a bark beetle infestation and other natural phenomena on forest impairment using a remote sensing-informed approach?

The ability of the proposed approach to detect the cause of forest impairment is limited. In some drastic, fast happening events affecting clusters of trees such as, for instance, in the case of storms or fires, the results are different form the ones obtained in an area primarily affected by bark beetles. Nevertheless, regionally and spatially more subtle events, such as drought stress, cannot be clearly discriminated from a bark beetle spread. Furthermore, the different factors interplay, as drought stress makes trees more vulnerable to insect infestations, and storms provide deadwood serving as easy accessible breeding ground for bark beetles.

Acknowledgements

I would like to express my appreciation to my supervisor, Prof. Dr. Alexander Damm, who found the right balance of leaving me the freedom to go after my own ideas while he always created a supportive and encouraging environment. Furthermore, I am grateful for having been given the opportunity to work in the Remote Sensing of Water Systems group during my master studies, allowing me an unforgettable behind the scenes insight into university life. I am grateful for the interesting projects, the numberless amazing discussions about work and life, days of fieldwork, coffee breaks, laughs and simply irreplaceable memories.
Additionally, I am grateful to have been able to collaborate with the team from the *Wildnispark Sihlwald*, especially Ronald, who elaborately answered all my questions and provided me with valuable information and high quality data to support my thesis. Also, Alex and I really enjoyed the possibility to go on a guided excursion with members of the *Sihlwald* team to gain expert insight into the on-site processes, for once from another perspective than the bird's eye view.
Moreover, my gratitude goes to Emiliano for his magic hands with code, for enduring countless discussions with a non-engineer and for thoroughly proofreading my thesis.
Furthermore, I want to thank Marius, for helping me with formatting the document with LaTeXand thus making my thesis interactively manageable and visually appealing.
Last but not least, I want to express my gratefulness towards my family for proofreading and sharing their non-remote sensing perspective on my thesis, and for having given me the possibility to study.

References

Abdullah, H., Skidmore, A. K., Darvishzadeh, R., and Heurich, M. (2019). Sentinel-2 accurately maps green-attack stage of European spruce bark beetle (Ips typographus, L.) compared with Landsat-8. *Remote Sensing in Ecology and Conservation*, 5(1):87–106.

Bazi, Y., Bruzzone, L., and Melgani, F. (2007). Image thresholding based on the EM algorithm and the generalized Gaussian distribution. *Pattern Recognition*, 40(2):619–634.

Bentz, B. J., Jönsson, A. M., Schroeder, M., Weed, A., Wilcke, R. A. I., and Larsson, K. (2019). Ips typographus and Dendroctonus ponderosae Models Project Thermal Suitability for Intra- and Inter-Continental Establishment in a Changing Climate. *Frontiers in Forests and Global Change*, 2(1):1–17.

Bentz, B. J., Régnière, J., Fettig, C. J., Hansen, E. M., Hayes, J. L., Hicke, J. A., Kelsey, R. G., Negrón, J. F., and Seybold, S. J. (2010). Climate Change and Bark Beetles of the Western United States and Canada: Direct and Indirect Effects. *BioScience*, 60(8):602–613.

Biedermann, P. H., Müller, J., Grégoire, J.-C., Gruppe, A., Hagge, J., Hammerbacher, A., Hofstetter, R. W., Kandasamy, D., Kolarik, M., Kostovcik, M., Krokene, P., Sallé, A., Six, D. L., Turrini, T., Vanderpool, D., Wingfield, M. J., and Bässler, C. (2019). Bark Beetle Population Dynamics in the Anthropocene: Challenges and Solutions. *Trends in Ecology & Evolution*, 34(10):914–924.

Bowker, D. E., Davis, R. E., Myrick, D. L., Stacy, K., and Jones, W. T. (1985). Spectral Reflectances of Natural Targets for Use in Remote Sensing Studies. Technical report, NASA National Aeronautics and Space Administration.

Brändli, K., Stillhard, J., Hobi, M., and Brang, P. (2020). Waldinventur 2017 im Naturerlebnispark Sihlwald. *WSL Berichte*, 93:1–52.

Copernicus (2014). Copernicus Open Access Hub. *https://scihub.copernicus.eu*, (Accessed: 02.04.2020).

de Groot, M. and Ogris, N. (2019). Short-term forecasting of bark beetle outbreaks on two economically important conifer tree species. *Forest Ecology and Management*, 450:117495.

Drusch, M., Del Bello, U., Carlier, S., Colin, O., Fernandez, V., Gascon, F., Hoersch, B., Isola, C., Laberinti, P., Martimort, P., Meygret, A., Spoto, F., Sy, O., Marchese, F., and Bargellini, P. (2012). Sentinel-2: ESA's Optical High-Resolution Mission for GMES Operational Services. *Remote Sensing of Environment*, 120:25–36.

ESA (2012). *Sentinel-2: ESA's Optical High-Resolution Mission for GMES Operational Services. European Space Agency ESA*. ESA Communications, Noordwijk.

Fassnacht, F. E., Latifi, H., Ghosh, A., Joshi, P. K., and Koch, B. (2014). Assessing the potential of hyperspectral imagery to map bark beetle-induced tree mortality. *Remote Sensing of Environment*, 140:533–548.

Fernandez-Carrillo, A., Patočka, Z., Dobrovolný, L., Franco-Nieto, A., and Revilla-Romero, B. (2020). Monitoring Bark Beetle Forest Damage in CentralEurope. A Remote Sensing Approach Validated withField Data. *Remote Sensing*, 12(21)(3634).

Frantz, D., Haß, E., Uhl, A., Stoffels, J., and Hill, J. (2018). Improvement of the Fmask algorithm for Sentinel-2 images: Separating clouds from bright surfaces based on parallax effects. *Remote Sensing of Environment*, 215:471–481.

Gao, B. C. (1996). NDWI - A normalized difference water index for remote sensing of vegetation liquid water from space. *Remote Sensing of Environment*, 58(3):257–266.

GIS Wildnispark Zürich (2015). Parkgrenze Wildnispark Zürich vom 24.05.2015. Wildnispark Zürich Data Center. *https://www.parcs.ch/wpz/mmd_fullentry.php?docu_id=32238*, (Accessed: 13.05.2020).

Gorelick, N., Hancher, M., Dixon, M., Ilyushchenko, S., Thau, D., and Moore, R. (2017). Google Earth Engine: Planetary-scale geospatial analysis for everyone. *Remote Sensing of Environment*, 202:18–27.

Gu, Y., Brown, J. F., Verdin, J. P., and Wardlow, B. (2007). A five-year analysis of MODIS NDVI and NDWI for grassland drought assessment over the central Great Plains of the United States. *Geophysical Research Letters*, 34(6).

Huang, Z. K. and Chau, K. W. (2008). A new image thresholding method based on Gaussian mixture model. *Applied Mathematics and Computation*, 205(2):899–907.

Jakus, R., Grodzki, W., Jezik, M., and Jachym, M. (2003). Definition of spatial patterns of bark beetle Ips typographus (L.) Outbreak spreading in tatra mountains (Central Europe), Using GIS. *Ecology, Survey and Management of Forest Insects*, 1-5:25–32.

Jensen, J. R. (2009). *Remote sensing of the environment: An earth resource perspective*. Pearson Education India.

Kanton Zürich (2018a). Geodatensatz Orthofoto Sommer RGB/Infrarot 2018. Geographisches Informationssystem GIS-ZH. *https://geolion.zh.ch/geodatensatz/show?giszhnr=493*, (Accessed: 13.04.2021).

Kanton Zürich (2018b). Geodatensatz Waldareal. Geographisches Informationssystem GIS-ZH. *https://geolion.zh.ch/geodatensatz/346*, (Accessed: 18.03.2021).

Kanton Zürich (2020). Geodatensatz Orthofoto Sommer RGB/Infrarot 2020. Geographisches Informationssystem GIS-ZH. *https://geolion.zh.ch/geodatensatz/show?giszhnr=527*, (Accessed: 13.04.2021).

Kautz, M., Dworschak, K., Gruppe, A., and Schopf, R. (2011). Quantifying spatio-temporal dispersion of bark beetle infestations in epidemic and non-epidemic conditions. *Forest Ecology and Management*, 262(4):598–608.

Khosravy, M., Gupta, N., Marina, N., Sethi, I. K., and Asharif, M. R. (2017). Morphological Filters: An Inspiration from Natural Geometrical Erosion and Dilation. In *Modeling and Optimization in Science and Technologies*, volume 10, pages 349–379. Springer Verlag.

Kottek, M., Grieser, J., Beck, C., Rudolf, B., and Rubel, F. (2006). World Map of the Köppen-Geiger climate classification updated. *Meteorologische Zeitschrift*, 15(3):259–263.

Lausch, A., Heurich, M., Gordalla, D., Dobner, H. J., Gwillym-Margianto, S., and Salbach, C. (2013). Forecasting potential bark beetle outbreaks based on spruce forest vitality using hyperspectral remote-sensing techniques at different scales. *Forest Ecology and Management*, 308:76–89.

Lillesand, T., Kiefer, R. W., and Chipman, J. (2015). *Remote Sensing and Image Interpretation*. John Wiley & Sons.

Marini, L., Økland, B., Jönsson, A. M., Bentz, B., Carroll, A., Forster, B., Grégoire, J. C., Hurling, R., Nageleisen, L. M., Netherer, S., Ravn, H. P., Weed, A., and Schroeder, M. (2017). Climate drivers of bark beetle outbreak dynamics in Norway spruce forests. *Ecography*, 40(12):1426–1435.

Martimort, P., Arino, O., Berger, M., Biasutti, R., Carnicero, B., Del Bello, U., Fernandez, V., Gascon, F., Greco, B., Silvestrin, P., Spoto, F., and Sy, O. (2007). Sentinel-2 optical high resolution mission for GMES operational services. In *International Geoscience and Remote Sensing Symposium (IGARSS)*, pages 2677–2680.

Martimort, P., Fernandez, V., Kirschner, V., Isola, C., and Meygret, A. (2012). Sentinel-2 MultiSpectral imager (MSI) and calibration/validation. In *International Geoscience and Remote Sensing Symposium (IGARSS)*, pages 6999–7002.

Marx, A. and An Der Havel, B. (2010). Erkennung von Borkenkäferbefall in Fichtenreinbeständen mit multi-temporalen RapidEye-Satellitenbildern und Datamining-Techniken. *Photogrammetrie • Fernerkundung • Geoinformation*, 4:243–252.

Matthews, B., Netherer, S., Katzensteiner, K., Pennerstorfer, J., Blackwell, E., Henschke, P., Hietz, P., Rosner, S., Jansson, P.-E., Schume, H., and Schopf, A. (2018). Transpiration deficits increase host susceptibility to bark beetle attack: Experimental observations and practical outcomes for Ips typographus hazard assessment. *Agricultural and Forest Meteorology*, 263:69–89.

Meigs, G. W., Kennedy, R. E., and Cohen, W. B. (2011). A Landsat time series approach to characterize bark beetle and defoliator impacts on tree mortality and surface fuels in conifer forests. *Remote Sensing of Environment*, 115(12):3707–3718.

MeteoSwiss (2018a). Der Wintersturm Burglind/Eleanor in der Schweiz. Federal Office of Meteorology and Climatology MeteoSwiss. *Fachericht MeteoSchweiz*, 268.

MeteoSwiss (2018b). Hitze und Trockenheit im Sommerhalbjahr 2018 - eine klimatologische Übersicht. Federal Office of Meteorology and Climatology MeteoSwiss. *Fachbericht MeteoSchweiz,*, 272.

MeteoSwiss (2018c). Klimabulletin Jahr 2017. Federal Office of Meteorology and Climatology MeteoSwiss. Zürich.

MeteoSwiss (2018d). Klimareport 2017. Federal Office of Meteorology and Climatology MeteoSwiss, Zürich, 84 P.

MeteoSwiss (2019a). Klimabulletin Jahr 2018. Federal Office of Meteorology and Climatology MeteoSwiss. Zürich.

MeteoSwiss (2019b). Klimareport 2018. Federal Office of Meteorology and Climatology MeteoSwiss, Zürich, 94 P.

MeteoSwiss (2020a). Klimabulletin Jahr 2019. Federal Office of Meteorology and Climatology MeteoSwiss. Zürich.

MeteoSwiss (2020b). Klimareport 2019. Federal Office of Meteorology and Climatology MeteoSwiss, Zürich, 96 P.

MeteoSwiss (2021a). Climate normals Wädenswil. Federal Office of Meteorology and Climatology MeteoSwiss. *https://www.meteoswiss.admin.ch/product/output/climate-data/climate-diagrams-normal-values-station-processing/WAE/climsheet_ WAE_ np6190_ e.pdf*, (Accessed: 29.04.2021).

MeteoSwiss (2021b). Klimabulletin Jahr 2020. Federal Office of Meteorology and Climatology MeteoSwiss. Zürich.

Millar, C. I. and Stephenson, N. L. (2015). Temperate forest health in an era of emerging megadisturbance.

Näsi, R., Honkavaara, E., Lyytikäinen-Saarenmaa, P., Blomqvist, M., Litkey, P., Hakala, T., Viljanen, N., Kantola, T., Tanhuanpää, T., and Holopainen, M. (2015). Using UAV-Based Photogrammetry and Hyperspectral Imaging for Mapping Bark Beetle Damage at Tree-Level. *Remote Sensing*, 7(11):15467–15493.

Nierhaus-Wunderwald, D. and Forster, B. (2004). Zur Biologie der Buchdruckerarten. *WSL Merkblatt für die Praxis*, 18:1–8.

Ortiz, S., Breidenbach, J., and Kändler, G. (2013). Early Detection of Bark Beetle Green Attack Using TerraSAR-X and RapidEye Data. *Remote Sensing*, 5(4):1912–1931.

Potterf, M. and Bone, C. (2017). Simulating bark beetle population dynamics in response to windthrow events. *Ecological Complexity*, 32:21–30.

Powell, J. A. and Logan, J. A. (2005). Insect seasonality: Circle map analysis of temperature-driven life cycles. *Theoretical Population Biology*, 67(3):161–179.

QGIS Development Team (2018). QGIS: A Free and Open Source Geographic Information System. version 3.4.12-Madeira. *Open Source Geospatial Foundation*.

Roy, D. P., Li, J., Zhang, H. K., and Yan, L. (2016). Best practices for the reprojection and resampling of Sentinel-2 Multi Spectral Instrument Level 1C data. *Remote Sensing Letters*, 7(11):1023–1032.

Schmitt, M., Hughes, L. H., Qiu, C., and Zhu, X. X. (2019). Aggregating Cloud-Free Sentinel-2 Images With Google Earth Engine. *ISPRS Annals of the Photogrammetry, Remote Sensing and Spatial Information Sciences*, 4(2/W7):145–152.

Schuldt, B., Buras, A., Arend, M., Vitasse, Y., Beierkuhnlein, C., Damm, A., Gharun, M., Grams, T. E., Hauck, M., Hajek, P., Hartmann, H., Hiltbrunner, E., Hoch, G., Holloway-Phillips, M., Körner, C., Larysch, E., Lübbe, T., Nelson, D. B., Rammig, A., Rigling, A., Rose, L., Ruehr, N. K., Schumann, K., Weiser, F., Werner, C., Wohlgemuth, T., Zang, C. S., and Kahmen, A. (2020). A first assessment of the impact of the extreme 2018 summer drought on Central European forests. *Basic and Applied Ecology*, 45:86–103.

Seidl, R. and Rammer, W. (2017). Climate change amplifies the interactions between wind and bark beetle disturbances in forest landscapes. *Landscape Ecology*, 32(7):1485–1498.

Seidl, R., Schelhaas, M. J., Lindner, M., and Lexer, M. J. (2009). Modelling bark beetle disturbances in a large scale forest scenario model to assess climate change impacts and evaluate adaptive management strategies. *Regional Environmental Change*, 9(2):101–119.

Senf, C. and Seidl, R. (2018). Natural disturbances are spatially diverse but temporally synchronized across temperate forest landscapes in Europe. *Global Change Biology*, 24(3):1201–1211.

Sidhu, N., Pebesma, E., and Câmara, G. (2018). Using Google Earth Engine to detect land cover change: Singapore as a use case. *European Journal of Remote Sensing*, 51(1):486–500.

Simard, M., Powell, E. N., Raffa, K. F., and Turner, M. G. (2012). What explains landscape patterns of tree mortality caused by bark beetle outbreaks in Greater Yellowstone? *Global Ecology and Biogeography*, 21(5):556–567.

Singh, P. and Komodakis, N. (2018). Cloud-GAN: Cloud removal for sentinel-2 imagery using a cyclic consistent generative adversarial networks. In *International Geoscience and Remote Sensing Symposium (IGARSS)*, volume July, pages 1772–1775. Institute of Electrical and Electronics Engineers Inc.

Skakun, S., Vermote, E., Roger, J. C., and Justice, C. (2017). Multispectral Misregistration of Sentinel-2A Images: Analysis and Implications for Potential Applications. *IEEE Geoscience and Remote Sensing Letters*, 14(12):2408–2412.

Skakun, S., Vermote, E. F., Artigas, A. E. S., Rountree, W. H., and Roger, J.-C. (2021). An experimental sky-image-derived cloud validation dataset for Sentinel-2 and Landsat 8 satellites over NASA GSFC. *International Journal of Applied Earth Observation and Geoinformation*, 95(102253).

Stereńczak, K., Mielcarek, M., Kamińska, A., Kraszewski, B., Piasecka, , Miścicki, S., and Heurich, M. (2020). Influence of selected habitat and stand factors on bark beetle Ips typographus (L.) outbreak in the Białowieża Forest. *Forest Ecology and Management*, 459:117826.

Stillhard, J., Brändli, K., Hobi, M., and Brang, P. (2020). Supplementary Data Sample Plot Inventory Sihlwald. *EnviDat*.

swisstopo (2018a). Swiss Map Raster 25: National mapping in digital raster format 1:25,000. Federal Office of Topography swisstopo. *https://www.swisstopo.admin.ch/en/geodata/maps/smr/smr25.html*, (Accessed: 23.04.2021).

swisstopo (2018b). Swiss Map Raster 50: National mapping in digital raster format 1:50,000. Federal Office of Topography swisstopo. *https://www.swisstopo.admin.ch/en/geodata/maps/smr/smr50.html*, (Accessed: 23.04.2021).

swisstopo (2019). swissALTI3D monodirectional hillshade: The high precision digital elevation model of Switzerland. Federal Office of Topography swisstopo. *https://test.map.geo.admin.ch/?lang=de&topic=ech&bgLayer=ch.swisstopo.pixelkarte-farbe&layers=ch.swisstopo.zeitreihen,ch.bfs.gebaeude_wohnungs_register,ch.bav.haltestellen-oev,ch.swisstopo.swisstlm3d-wanderwege,ch.swisstopo.swissalti3d-reliefschattierung_*, (Accessed: 29.04.2021).

swisstopo (2020). Pixelkarte mit Flurnamen. Federal Office of Topography swisstopo. *https://map.geo.admin.ch*, (Accessed: 13.04.2021).

The MathWorks Inc. (2019). MATLAB version R2019a (9.6.0.1072779). *Natick, Massachusetts.*

Valdez Vasquez, M. C., Chen, C. F., Lin, Y. J., Kuo, Y. C., Chen, Y. Y., Medina, D., and Diaz, K. (2020). Characterizing spatial patterns of pine bark beetle outbreaks during the dry and rainy season's in Honduras with the aid of geographic information systems and remote sensing data. *Forest Ecology and Management*, 467:118162.

Wermelinger, B. (2004). Ecology and management of the spruce bark beetle Ips typographus - A review of recent research. *Forest Ecology and Management*, 202(1-3):67–82.

Wermelinger, B. (2020). Der Borkenkäfer - Altes, Neues, Wissenswertes. *Zürcher Wald*, 1:22–26.

Wulder, M. A., Dymond, C. C., White, J. C., Leckie, D. G., and Carroll, A. L. (2006). Surveying mountain pine beetle damage of forests: A review of remote sensing opportunities. *Forest Ecology and Management*, 221(1-3):27–41.

Zhu, Z., Wang, S., and Woodcock, C. E. (2015). Improvement and expansion of the Fmask algorithm: Cloud, cloud shadow, and snow detection for Landsats 4-7, 8, and Sentinel 2 images. *Remote Sensing of Environment*, 159:269–277.

Personal Declaration

I hereby declare that the submitted thesis is the result of my own, independent work. All external sources are explicitly acknowledged in the thesis.

Zürich, 30.04.2021

Place, Date

Signature